In-situ electro-generation and activation of hydrogen peroxide using a CuFeNLDH-CNTs modified graphite cathode for degradation of cefazolin

Ghasemi, Masoumeh

2020-08-01

In-situ electro-generation and activation of hydrogen peroxide using a CuFeNLDH-CNTs modified graphite cathode for degradation of cefazolin

Masoumeh Ghasemi,[b] Alireza Khataee,[b, c, d*] Peyman Gholami,[b, e] Reza Darvishi Cheshmeh Soltani,[f] Aydin Hassani,[g] Yasin Orooji,[a,*]

[a] College of Materials Science and Engineering, Nanjing Forestry University, Nanjing 210037, China

[b] Research Laboratory of Advanced Water and Wastewater Treatment Processes, Department of Applied Chemistry, Faculty of Chemistry, University of Tabriz, 51666-16471 Tabriz, Iran

[c] Department of Environmental Engineering, Gebze Technical University, 41400 Gebze, Turkey

[d] Institute of Research and Development, Duy Tan University, Da Nang 550000, Vietnam

[e] Department of Chemistry, University of Helsinki, P.O. Box 55, Helsinki 00014, Finland

[f] Department of Environmental Health Engineering, School of Health, Arak University of Medical Sciences, 38196-93345 Arak, Iran

[g] Department of Materials Science and Nanotechnology Engineering, Near East University, 99138 Nicosia, TRNC, Mersin 10, Turkey

* Corresponding authors:

Email: a_khataee@tabrizu.ac.ir (A. Khataee)

yasin@njfu.edu.cn (Y. Orooji)

Abstract

The modified multifunctional electrodes for electro-Fenton (EF) process are suggested to be promising cathodes for in situ electro-generation and activation of H_2O_2 to produce hydroxyl radicals ($^\bullet OH$). However, heterogeneous EF process still faces the challenges of limited catalytic activity and releasing of massive amounts of transition metals to the solution after removal of organic pollutants. The main aim of the present investigation was to prepare a cathode containing carbon nanotubes (CNTs) and CuFe nano-layered double hydroxide (NLDH) for degradation and mineralization of cefazolin antibiotic through electro-Fenton process. Structural and electrochemical analyses demonstrated that CuFeNLDH-CNTs nanocomposite was successfully incorporated on the surface of graphite cathode. Due to the increased formation of $^\bullet OH$ in the reactor, the incorporation of CNTs into NLDH matrix with a catalyst loading of 0.1 g substantially improved the degradation efficiency of cefazolin (89.9%) in comparison with CNTs-coated (28.7%) and bare graphite cathode (22.8%) within 100 min. In the presence of 15 mM of ethanol, the degradation efficiency of cefazolin was remarkably decreased to 43.7% by the process, indicating the major role of $^\bullet OH$ in the destruction of target molecules. Acidic conditions favored the degradation efficiency of cefazolin by the modified EF process. Mineralization efficiency of the bio-refractory compound was obtained to be 70.1% in terms of chemical oxygen demand (COD) analysis after 300 min. The gas chromatography-mass spectroscopy (GC-MS) analysis was also implemented to identify the intermediate byproducts generated during the degradation of cefazolin in the CuFeNLDH-CNTs/EF reactor.

1. Introduction

In recent years, the discharge of wastewaters containing pharmaceutical compounds into aquatic ecosystems has become a great environmental and health concern [1, 2]. Among various groups of pharmaceuticals, antibiotic compounds have been further considered because of their wide implementation for the treatment of bacterial-causing infections [3, 4]. A typical antibiotic model is cefazolin, which is a part of β-lactam cephalosporines antibiotics derived from the *Cephalosporium* fungus. It is a semi-synthetic compound manufactured for the treatment of acute infections in bones, stomach, heart valves and lungs [5, 6].

Noticeably, even trace amounts of β-lactam antibiotics such as cefazolin in water resources and wastewater treatment plants effluents may lead to adverse effect on aquatic life and subsequently human life [7, 8]. In addition, the presence of antibiotics such as cefazolin in the ecosystem will lead to the development of antibiotic-resistant microbial strains [9]. Microbial resistance against antibiotic drugs has become a major global health concern [10]. Since most antibiotics are categorized as recalcitrant compounds, biological treatment processes are not able to efficiently degrade this type of contaminants [11].

Application of efficient chemical treatment processes, especially advanced oxidation processes (AOPs) has been considered for effective destruction and mineralization of these bio-refractory compounds [12-14]. The implementation of AOPs results in the formation of hydroxyl radical ($^{•}OH$) with high oxidation potential to non-selectively degrade various organic and inorganic substances [15]. Many AOPs have been examined for treating antibiotic compounds. Among them, due to their high effectiveness and low operational (annual) costs, Fenton-based treatment processes and in particular, Fenton's reaction-based electrochemical advanced oxidation processes (EAOPs) have been successfully utilized for the decontamination of antibiotic-polluted water streams [11, 16]. The efficiency of the electro-

74 Fenton (EF) process is significantly affected by the capability of the process to in situ generate

75 H_2O_2 through the cathodic reduction as shown in the following reaction [11]:

76 $$O_2 + 2H^+ + 2e^- \rightarrow H_2O_2 \qquad (1)$$
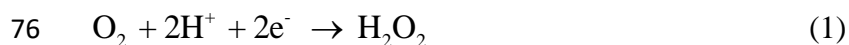
77 In the following, the as-generated H_2O_2 molecules react with iron ions as Fenton catalyst to

78 produce $^\bullet OH$ in the bulk solution [17]:

79 $$Fe^{2+} + H_2O_2 + H^+ \rightarrow Fe^{3+} + {}^\bullet OH + H_2O \qquad (2)$$
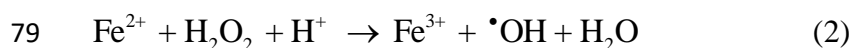
80 According to the previous studies, efficient generation of H_2O_2 in EF process can be

81 attained by the immobilization of carbonaceous nanostructures such as carbon nanotubes

82 (CNTs) on the graphite cathode surface [18, 19]. CNTs can offer important benefits for the

83 two-electron reduction of oxygen owing to their good surface activity, high electrical

84 conductivity, and mechanical strength [19]. On the other hand, as an innovative method, the

85 catalyst is immobilized on the cathode surface to continuously generate $^\bullet OH$ in the bulk

86 solution. Based on this approach, the stability of the EF process in repeated runs will be

87 increased as well as its cost-effectiveness. Iron ions are constantly regenerated on the surface

88 of the catalyst-coated cathode.

89 Layered double hydroxides (LDHs) are one of the most useful classes of inorganic layered

90 compounds which can be used to host heterogeneous Fenton catalysts on the surface of cathode,

91 improving its structure for the in-situ generation of H_2O_2 and subsequently, the formation of

92 $^\bullet OH$ during the EF process. Due to their versatility as well as their unique structure with high

93 porosity and thermal stability, LDHs and their modifications have been extensively utilized as

94 heterogeneous catalysts for numerous applications [20, 21].

95 In this study, Fe together with Cu ions was incorporated into LDH matrix as Fenton

96 reaction's catalysts to avoid the leachate of toxic Fe and Cu ions into the ecosystem.

97 Considering the advantages of nano-materials, the nano-LDH (NLDH) containing Fe and Cu

98   nanostructures was used as an active site to catalyze the generation of free oxidizing agents for

99   the decomposition of target contaminants. CNTs were added to the CuFeNLDH-coated cathode

100 to produce more oxidizing radicals in the solution for the degradation of cefazolin antibiotic.

101 The as-synthesized cathode was characterized by using scanning electron microscopy (SEM),

102 high resolution transmission electron microscopy (HR-TEM), X-ray diffraction (XRD),

103 Fourier transform infrared spectroscopy (FT-IR), Energy-dispersive X-ray spectroscopy

104 (EDX) equipped with elemental mapping, X-ray photoelectron spectroscopy (XPS), cyclic

105 voltammetry (CV), and linear scan voltammetry (LSV) analyses. Hitherto, no study has been

106 performed and reported regarding the application of CuFeNLDH/CNTs-coated graphite as

107 nanocomposite cathode for the EF process to decontaminate polluted water streams. Chemical

108 oxygen demand (COD) and gas chromatography-mass spectrometry (GC–MS) analyses were

109 also performed to determine the mineralization rate and intermediate byproducts during the

110 degradation of cefazolin.

111

112 2. Materials and methods

113 2.1. Chemicals

114   Copper (II) nitrate trihydrate ($Cu(NO_3)_2.3H_2O$: 90%), iron (III) nitrate hexahydrate

115 ($Fe(NO_3)_3.6H_2O$: 99%), ammonium fluoride (NH_4F: 95%), hydrochloric acid (HCl: 37%),

116 sodium sulfate (Na_2SO_4: 98.5%), hydrogen peroxide (H_2O_2: 35%), sodium carbonate (Na_2CO_3:

117 98%), nitric acid (HNO_3: 65%), sulfuric acid (H_2SO_4: 98%), ethanol (C_2H_5OH: 96%), urea

118 (CH_4N_2O: 99.5%),   1,4-benzoquinone ($C_6H_4O_2$: 99%), n-butanol ($C_4H_{10}O > 99.7\%$) and

119 sodium hydroxide (NaOH: 99%) were obtained from Merck (Germany). Pristine multi-walled

120 carbon nanotubes (MWCNTs) with 3-5 nm inner diameter and 8-15 nm outer diameter were

121 obtained from Cheap Tubes (USA). 60% polytetrafluoroethylene (PTFE) solution (Teflon

122   Dispersion, DISP 30) was purchased from DuPont (USA). Graphite plates were purchased

123   from Tabriz Zoghal Co. (Iran). Cefazolin was obtained from Loghman Co. (Iran). The

124   characteristics and chemical structure of cefazolin are presented in Table 1.

125

2.2. Modification of CNTs

127   For the addition of hydroxyl and carboxyl groups onto the surface of CNTs, a mixture of

128   pristine CNTs and 1: 3 volume ratio of nitric acid and sulfuric acid were sonicated at 80.0 $\pm$

129   0.5 ℃ for 1 h. After washing with deionized water and centrifugation with 3500 $\pm$ 50 rpm for

130   30 min, the acid-treated CNTs were dried at 60.0 $\pm$ 0.5 °C for 12 h (Fig. S1).

131

2.3. Synthesis of CuFeNLDH-CNTs

133   The CuFeNLDH-CNTs nanocomposite was synthesized by the hydrothermal method.

134   Appropriate amounts of $Cu(NO_3)_2.3H_2O$ (250.0 mmol/L), $Fe(NO_3)_3.6H_2O$ (125.0 mmol/L),

135   NH_4F (312.5 mmol/L), Urea (1250.0 mol/L) and modified CNTs (0.5 g) were mixed in 70 mL

136   deionized water. The resulting solution was stirred with a magnetic stirrer for 30 min. After

137   that, the obtained solution was transferred into a 100 mL Teflon-lined stainless steel autoclave.

138   The sealed autoclave was placed in an oven and kept at 90.0 $\pm$ 0.5 °C for 24 h. Finally, as-

139   synthesized CuFeNLDH-CNTs crystals were dried at 50.0 $\pm$ 0.5 ℃ after five times washing

140   (Fig. S2).

141

2.4. Immobilization of CuFeNLDH-CNTs on the graphite plate

143   In order to clean the surface of the graphite plate, it was immersed in a solution of 10%

144   nitric acid and sonicated using a probe sonicator (Hielscher, UP400S, 400 W, 24 kHz) for 30

145   min. Firstly, 1.4 g PTFE and 0.1 g CuFeNLDH-CNT were added to the mixture of water (30

146   mL) and n-butanol (6% w/w). The obtained suspension was sonicated for 30 min to obtain a

147   highly dispersed mixture. The resulting mixture was heated at 80.0 ± 0.5 °C until an ointment

148   appeared. The resulting ointment was immobilized on the graphite plate and was calcined at

149   350 ± 5 °C for 15 min under nitrogen gas. PTFE in the cathode has two roles: pasting the high

150   surface CuFeNLDH-CNTs into a cohesive layer and imparting some hydrophobic character to

151   the layer. Schematic diagram for the stabilization of nanocomposite on the graphite plate is

152   shown in Fig. S3.

153

2.5. Characterization

155   XRD analysis (PANalytical X'Pert PRO, Germany) with Cu Kα radiation ($\lambda = 0.15406$ nm)

156   was used to determine the crystallite structure of the treated graphite plate at 40 mA and 45 kV.

157   The functional groups of CuFeNLDH, CNTs and CuFeNLDH-CNTs were analyzed by FT-IR

158   spectrometer (Tensor 27, Bruker, Germany), with the KBr pellet in the range of 400–4000 cm^{-1}

159   ^{1}. The surface morphology, magnitudes and chemical composition of CuFeNLDH, CNTs,

160   CuFeNLDH-CNTs and the treated graphite electrode were examined by SEM equipped with

161   EDX spectroscopy (Mira3 FEG-SEM Tescan, Czech Republic). HR-TEM images were taken

162   by a high resolution microscope (Hitachi HT-7700, Japan) operating at 120 kV. CV (scan rate

163   of 50 mV/s) and LSV were performed using an electrochemical system (PG-Stat 30,

164   Netherlands). XPS spectra were also recorded using Kratos AXIS UltraDLD spectrometer

165   (UK).

166

167

2.6. Apparatus and analyses

169   For EF experiments, the anode was a platinum sheet (6.25 cm^2) and the cathode was the

170   CuFeNLDH-CNTs-coated graphite plate (3 cm^2). The distance between the platinum sheet and

171 the treated graphite plate was 1 cm. EF experiments were done at room temperature (25.0 ± 0.5

172 °C) using an undivided cylindrical glass reactor containing 80 mL cefazolin-contained solution

173 as the target pollutant and Na_2SO_4 as the supporting electrolyte with certain concentrations.

174 Both electrodes were connected to a DC power supply (Adak PS-808, Iran). During the reaction

175 time, an air pump (RS-510, China) was used for air injection into the reactor. Ozone gas (ozone

176 generator, BE-72, Iran) was bubbled into the bulk solution by means of a porous diffuser. It

177 was coupled with an oxygen concentrator (Airsep, USA). The cefazolin degradation was

178 measured by determining the absorbance at a wavelength of 260 nm with a UV-Vis

179 spectrophotometer (SU–6100, Philler scientific, USA). The concentration of H_2O_2 electro-

180 generated on the surface of bare graphite electrode and modified electrodes were determined

181 by the iodide method [22]. The COD concentration before the treatment process and the

182 residual COD after the treatment process were determined by a standard method (method no.

183 5220) [23], using Palin test (United Kingdom) apparatus. The intermediates produced during

184 the cefazolin degradation were determined by Agilent 6890 gas chromatography-mass

185 spectrometry (GC–MS) and an Agilent 5973 mass spectrometer (Canada).

186

3. Results and discussion

3.1. Characterization

3.1.1. SEM images

190 Fig. 1 exhibits the SEM images of CuFeNLDH (a-d), pristine CNTs (e-h), CuFeNLDH-

191 CNTs nanocomposite (i-l) and CuFeNLDH-CNTs-coated graphite cathode (m-p). As can be

192 seen in Fig. 1 (a-d), CuFeNLDH consists of microspheres decorated with nano-sheets with an

193 average diameter of 26 nm. The SEM images of CuFeNLDH-CNTs nanocomposite display

194 that CNTs are successfully incorporated into CuFeNLDH nano-sheets (Fig. 1 (i-l)).

195 CuFeNLDH-CNTs nanocomposite coated on graphite plate can be also observed in Fig. 1 (m-

196 p). The presence of nano-tubes in the structure of CuFeNLDH-CNTs nanocomposite

197 immobilized on the surface of graphite cathode can be clearly seen in Fig. 1 (o and p).

198

199 **3.1.2. EDX spectra**

200 EDX spectroscopy equipped with SEM analysis was implemented to specify elemental

201 composition of CuFeNLDH, CNTs, CuFeNLDH-CNTs and CuFeNLDH-CNTs-coated

202 graphite cathode (Fig. S4 (a-d)). The results revealed that the CuFeNLDH contained O, N, C,

203 Cu and Fe elements (Fig. S4 (a)). According to Fig. S4 (b), the CNTs is composed of C and O

204 elements. Compared with non-immobilized CuFeNLDH-CNTs, the amount of C element in

205 the structure of the modified cathode remarkably increased due to the immobilization of

206 CuFeNLDH-CNTs on the surface of graphite cathode. The elemental mapping images of

207 CuFeNLDH/CNTs-coated graphite cathode was also performed (Fig. S5). As shown, the

208 elements in the composition of the modified cathode are uniformly distributed, indicating the

209 suitable structure of as-synthesized cathode for the reduction of oxygen molecule and

210 generation of $^\bullet$OH via the whole surface of cathode through the interaction of Cu and Fe ions

211 with electro-generated H_2O_2.

212

213 **3.1.3. HR-TEM images**

214 HR-TEM images of CuFeNLDH and CuFeNLDH-CNTs are exhibited in Fig. 2. Fig. 2 (a

215 and b) indicates the formation of sheet-like CuFeNLDH nanostructures with regular size and

216 relatively uniform size distribution. The size of thickness and width of CuFeNLDH

217 nanostructures are in the range of 10.00-30.00 and 20.00-50.00 nm, respectively (Fig. 2 (e and

218 f)). The images of CNTs-implanted CuFeNLDH show the presence of ultrafine structures in

219 the composition of nanocomposite (Fig. 2 (c and d)), creating high surface area and more

220 reaction sites for the generation of H_2O_2 molecules and $^\bullet$OH radicals to catalytically convert

221   the target antibiotic pollutant. Fig. 2 (d) displays that CNTs are successfully introduced into

222   the CuFeNLDH nano-sheets.

223

3.1.4. XRD patterns

225   The XRD patterns of CuFeNLDH, CuFeNLDH-CNTs, and CuFeNLDH-CNTs-coated

226   graphite are shown in Fig. 3 (a-c). For the XRD pattern of CuFeNLDH (Fig. 3a), characteristic

227   peaks placed at 12.8, 25.8, 33.6, 36.5 and 43.2° correspond to the (003), (006), (012), (015)

228   and (018) crystal plane according to JCPDS card no. 41-1428 [24]. In the case of XRD patterns

229   obtained for CuFeNLDH-CNTs (Fig.3b) and CuFeNLDH-CNTs-coated graphite (Fig.3c), the

230   diffraction peak located at about 26.5° is associated with the (002) reflection of the CNTs and

231   graphite based on JCPDS card no. 74-444 [25].

232

3.1.5. FT-IR spectra

234   The FT-IR spectra of CuFeNLDH, CNTs and CuFeNLDH-CNTs samples are displayed in

235   Fig. S6. FT-IR spectrum of CuFeNLDH exhibits the peaks at 464 and 582 cm^{-1} attributed to

236   the Fe-O vibration [26]. The peak placed at 518 cm^{-1} indicates the Cu-O bond [27]. A broad

237   and intense peak was observed at 3452 cm^{-1}, related to the O-H stretching vibration [28, 29].

238   The weak peaks located at 2854 to 2925 cm^{-1} are ascribed to symmetric and asymmetric

239   stretching of C-H bond, respectively [30]. Moreover, the peaks at 1386, 1687 and 875 cm^{-1} can

240   be related to C-N, C=O and C-O vibrations, respectively [31, 32]. The peaks for C=O vibration

241   (1645 cm^{-1}) and C-N vibration (1126 cm^{-1}) can be observed in the spectrum of the modified

242   CNTs [33]. As mentioned, the peak at 3458 cm^{-1} represents the O-H group in the structure of

243   CuFeNLDH-CNTs [34]. However, CuFeNLDH-CNTs spectrum shows an absorption band at

244   516 cm^{-1} attributed to Cu-O vibrations [26] and a peak at 680 cm^{-1} related to Fe-O vibration

245   [35].

3.1.6. XPS

XPS analysis was performed for CuFeNLDH, CuFeNLDH/CNTs, and CuFeNLDH-CNTs-coated graphite cathode whose results are presented in Fig. 4. As can be seen in XPS full spectra of the samples (Fig. 4 (a-c)), CuFeNLDH is composed of O (39.53%), Cu (27.37%), Fe (15.71%), C (12.46%) and N (4.93%) elements. CuFeNLDH/CNTs sample contains O, Cu, Fe, C and N elements with 38.42, 18.82, 8.71, 30.13 and 3.92 atomic percent (At%), respectively. The higher At% of carbon in the structure of the modified cathode compared with CuFeNLDH/CNTs sample is owing to the immobilization of CuFeNLDH-CNTs on the surface of graphite cathode. It was found that the Fe/Cu At% ratio in CuFeNLDH, CuFeNLDH/CNTs, and CuFeNLDH-CNTs-coated graphite cathode was 0.57, 0.46 and 0.53 which is in good accordance with 1/2 molar ratio of iron/copper precursors utilized in the preparation of the samples. High-resolution XPS spectra of Fe 2p, Cu 2p and O 1s are shown in Fig. 4 (d-l). Fig. 4 (d and e) shows the presence of three peaks at ~712, ~719 and ~725 eV, which are attributed to Fe 2p1/2, Fe 2p3/2 and their satellite, demonstrating that the main part of iron in the structure of CuFeNLDH and CuFeNLDH/CNTs samples is in trivalent state [36]. After immobilizing CuFeNLDH/CNTs on the graphite surface, the peak at ~719 eV nearly disappeared and a new peak was observed at ~708 eV corresponding to Fe^{2+} ion (Fig. 4 (d-l)) [37]. This observation demonstrated that a part of Fe^{3+} in the structure of CuFeNLDH was reduced to Fe^{2+} during the calcination of the CuFeNLDH/CNTs-modified electrode at 350 ± 5 °C under nitrogen atmosphere. The Cu 2p XPS spectra of CuFeNLDH and CuFeNLDH/CNTs (Fig. 4 (g and h)) exhibit the peaks at ~935, ~942, ~955 and ~962 eV which illustrate copper oxidation state of 2+ [38]. Compared with CuFeNLDH and CuFeNLDH-CNTs, the intensities of the peaks observed in high-resolution spectrum of Fe 2p were considerably decreased for CuFeNLDH-CNTs-coated graphite (Fig. 4 (f)) and Cu 2p peaks became indistinguishable from background

271   noise (Fig. 4 (i)). This can be related to the immobilization of CuFeNLDH-CNTs on the

272   graphite plate using PTFE binder which leads to a decrease in Fe and Cu contents and the

273   variation of their surrounding electron density due to the presence of adjacent species [39, 40].

274   As shown in high-resolution XPS spectra of O 1s (Fig. 4 (j-l)), there is a single peak at binding

275   energy of ∼533 eV which can be ascribed to OH^- belonging to metal hydroxides or hydroxyl

276   groups [41].

277

278   **3.1.7. CV and LSV curves**

279   The electrochemical performance of the bare graphite cathode was compared with graphite

280   cathodes modified with CuFeNLDH/CNTs nanocomposite using cyclic voltammetry (CV)

281   analysis. Fig. 5 (a) and (b) show the results of CV analysis carried out in the potential range of

282   -0.7-1.0 V with a scan rate of 50.0 mV/s in N_2- and O_2-saturated solutions, respectively. A

283   reduction peak was detected at the potential around –0.1 V in oxygen saturated solution.

284   However, no obvious reduction peak was observed for N_2 saturated solution, and its reductive

285   current was slightly lower than that of in O_2-saturated solution, revealing that the prepared

286   cathodes had high activity toward oxygen reduction. On the other hand, the graphite cathodes

287   modified with CuFeNLDH/CNTs nanocomposite have a higher oxygen evolution potential

288   than that of the bare graphite cathode. Linear scan voltammetry (LSV) analysis was also used

289   to further evaluate the electrochemical properties of the modified graphite cathodes in

290   comparison with the bare cathode (Fig. 5 (c)). Accordingly, the results of LSV analysis verified

291   the results of CV analysis. The high oxygen evolution potential of the cathodes leads to the

292   increased generation of hydrogen peroxide and subsequently, increased $^•OH$ in the bulk

293   solution. Moreover, high oxygen evolution potential reduces power loss during the

294   electrochemical-based treatment process, leading to the enhanced cost-effectiveness of the

295   process and its current efficiency [42]. At a specified potential, lower increase in the current of

296   graphite cathodes modified with CuFeNLDH/CNTs nanocomposite was obtained in

297   comparison with that of the bare cathode. The electroactive surface area of the electrodes were

298   determined in the ferrocyanide system ($[Fe(CN)_6]^{3-}/[Fe(CN)_6]^{4-}$) based on the Randles-Sevcik

299   equation (Eq. 3) [43]:

300    $I_p = 2.69 \times 10^5 \times AD^{1/2}n^{3/2}\gamma^{1/2}C$ (3)

301   where Ip is the peak current (A), A is the geometric area of the electrode (cm^2), D is the

302   diffusion coefficient of the probe molecule (7.60×10^{-6} cm^2 s^{-1}), C is the concentration of

303    $[Fe(CN)_6]^{4-}$ in solution (1×10^{-5} mol/cm^{-3}), n = 1 is the number of electrons involved in the

304   redox Fe^{III}/Fe^{II} reaction and γ is the scan rate (0.05 V s−1). As displayed in Fig. 5 (b), the peak

305   currents of both graphite/CNTs (0.1 g) and graphite/NLDH-CNTs (0.1 g), were higher than

306   that of bare graphite cathode. Accordingly, electroactive surface area was calculated as 5.61,

307   8.82 and 8.29 for the bare graphite, graphite/CNTs (0.1 g) and graphite/NLDH-CNTs (0.1 g),

308   respectively. The electroactive surface area is one of the important characteristics of the

309   cathode that can potentially enhance the efficiency of the EF process in terms of hydrogen

310   peroxide generation.

311

312   **3.2. Comparison of the performance of different electrodes**

313   A comparative study was performed before the evaluation of the effect of the main

314   operational parameters on the efficiency of the treatment process. The results of these

315   preliminary experiments are provided in Fig. 6 (a). Based on the data obtained, the

316   immobilization of CNTs on the surface of the bare cathode resulted in an insignificant increase

317   in the degradation efficiency of cefazolin compared with the bare cathode (increasing from

318   22.8% to 28.7%). Interestingly, an obvious increase in the degradation of cefazolin occurred

319   when the CNTs were incorporated into CuFeNLDH lattice. Due to the facile interchangeability

320   of implanted anions and uniform distribution of metal cations in the brucite-like layers of the

13

321 compound, LDHs exhibit catalytic activity as semiconductor with high stability to be used in

322 various systems including catalytic treatment processes [44]. Particularly, Fe together with Cu

323 ions which are incorporated into LDH matrix act as Fenton reaction's catalysts [20]; thus, the

324 presence of these ions in the structure of LDH leads to the formation of $^{\bullet}OH$ through the

325 interaction with as-generated H_2O_2 molecules, which resulted in the enhanced degradation

326 efficiency of cefazolin antibiotic by the electro-Fenton process in comparison with the

327 application of CNTs alone. However, an optimum amount of CuFeNLDH-CNTs

328 nanocomposite immobilized on the cathode surface is required to attain the maximum

329 efficiency. The degradation efficiency of cefazolin increased from 48.0% to 69.8% when the

330 amount of CuFeNLDH-CNTs increased from 0.05 to 0.10 g, respectively; while increasing the

331 amount of CuFeNLDH-CNTs up to 0.15 g led to a slight decrease in the degradation efficiency

332 of the pollutant (66.3%). Although the efficiency of CuFeNLDH/CNTs-equipped electro-

333 Fenton process for the degradation of target compound can be enhanced by increasing the

334 amount of coated catalyst; however, increasing the amount of CuFeNLDH/CNTs may cause

335 mass transfer limitation on the cathode surface [45], leading to the reduced formation of

336 oxidizing agents in the electrochemical cell. Moreover, the aggregation of coated catalyst on

337 the surface of the cathode is inevitable at higher amounts which may be the dominating factors

338 leading to the loss of catalyst [46]. Overall, the agglomeration of catalyst or increasing the

339 thickness of the coated catalyst leads to the reduced reactive sites for the reduction of diffused

340 oxygen molecules. Furthermore, protons with small size and high mobility can permeate into

341 the thin film of the catalyst better than the thick layer [47]. Therefore, in the present study, the

342 catalyst loading of 0.10 g was considered as the optimum value in comparison with other values

343 (0.05 and 0.15 g) considering economic and applicability point of view. Fig. 6 (b) shows the

344 concentration of H_2O_2 produced during the EF process on the bare graphite cathode, CNTs-

345 coated graphite and graphite cathodes modified with different amounts of CuFeNLDH/CNTs

346 nanocomposite. Comparatively, the amount of electro-generated H_2O_2 decreased when the

347 cathode surface was coated with CuFeNLDH/CNTs in comparison with the bare and CNTs-

348 coated graphite. This can be due to the interaction of electro-generated H_2O_2 with Fe and Cu

349 ions in the structure of NLDH, thereby producing $^\bullet OH$ and $HO_2^\bullet$ radicals in the solution for the

350 efficient degradation of cefazolin according to Eqs. (4-7) [48]:

351 $$Fe^{3+} + H_2O_2 \rightarrow Fe^{2+} + HO_2^\bullet + H^+ \qquad (4)$$

352 $$Fe^{2+} + OH^\bullet \rightarrow Fe^{3+} + OH^- \qquad (5)$$

353

354 $$Cu^{2+} + H_2O_2 \rightarrow Cu^+ + HO_2^\bullet + H^+ \qquad (6)$$

355 $$Cu^+ + H_2O_2 \rightarrow Cu^{2+} + OH^- + OH^\bullet \qquad (7)$$

356

357   Based on the above reactions, the presence of CuFeNLDH on the cathode surface inhibits

358 the accumulation of H_2O_2 molecules in the bulk solution. During the EF process, recycling

359 potential of iron species can easily take place through the following equation:

360 $$Fe(III) + e^- \rightarrow Fe(II) \qquad (8)$$

361   As-converted Fe(II) can directly react with hydrogen peroxide to produce $^\bullet OH$ radicals and

362 concurrently be converted to Fe(III) ions. That is why the major oxidizing agent in the

363 CuFeNLDH-CNTs/EF reactor was still $^\bullet OH$ radicals. It should not be overlooked that part of

364 hydrogen peroxide molecules may be oxidized on the surface of Pt anode, generating oxygen

365 molecules in the EF reactor [49]:

366 $$H_2O_2 \rightarrow O_2 + 2H^+ + 2e^- \qquad (9)$$
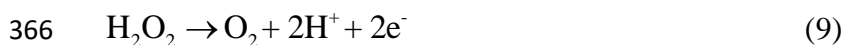
367

368

369 **3.3. Effect of operational parameters**

370   The effect of initial pH on the degradation efficiency of cefazolin is displayed in Fig. 7 (a).

371   As shown, the acidic conditions favored the removal of target pollutant by the CuFeNLDH-

372   CNTs/EF process. An increase in the initial pH from 3.0 to 11.0 led to a decrease in removal

373   efficiency from 95.8% to 53.3%, respectively. Actually, the formation of hydrogen peroxide

374   through cathodic reduction is increased under acidic conditions, thereby leading to enhanced

375   production of $^{\bullet}$OH in the CuFeNLDH-CNTs/EF reactor. Based on Fig. 7 (a), the change in the

376   degradation efficiency of cefazolin was not significant in the pH range of 3.0-6.0 (decreasing

377   from 95.8% to about 90.0%); thus, the pH value of 6.0 was chosen as the selective pH for

378   conducting the rest of the experiments, while taking cost-efficiency of the treatment system

379   into account. The effect of the applied current on the degradation efficiency of cefazolin by the

380   EF process was assessed (Fig. 7 (b)). Obviously, increasing the applied current in the range of

381   150.0-400.0 mA resulted in the enhanced degradation efficiency of cefazolin from 39.7% to

382   92.8% over the reaction time of 100 min. However, as shown in Fig. 7 (b), increasing the

383   current from 300.0 to 400.0 mA did not significantly influence the efficiency of the EF process

384   (not more than 3.0% increase in the degradation efficiency). In fact, the efficiency of the

385   process operated at these two applied currents was almost the same. Thus, the current intensity

386   of 300.0 mA was considered in the following experimental runs. The application of higher

387   applied currents results in the in-situ generation of more free radicals through the

388   CuFeNLDH/CNTs-coated graphite cathode [50]. Furthermore, increasing the current intensity

389   quickens the diffusion rate of the reactants in the bulk solution, bringing about the improved

390   efficiency of the EF reactor. The results of the effect of cefazolin concentration on its

391   degradation efficiency are presented in Fig. 7 (c). As a result, the degradation efficiency

392   decreased from 45.78% to 95.5% as the initial concentration of cefazolin decreased from 40.0

393   to 10.0 mg/L, respectively. Clearly, higher amounts of oxidizing agents are required to treat

394   the solution containing higher concentrations of cefazolin to attain the pre-determined

16

395 efficiency [51]. The effect of supporting electrolyte concentration on the degradation efficiency

396 of cefazolin was also examined by varying the sodium sulfate concentration in the range of

397 25.0-100.0 mmol/L. According to Fig. 7 (d), rapid increase in the degradation efficiency of

398 cefazolin from 59.5% to about 90.0% was observed when the supporting electrolyte

399 concentration increased from 25.0 to 50.0 mmol/L; while, increasing its concentration from

400 50.0 to 75.0 mmol/L did not meaningfully influence the efficiency of the EF process over the

401 reaction time of 100 min. Noticeably, increasing the electrolyte concentration from 75.0 to

402 100.0 mmol/L led to a substantial decrease in the degradation efficiency of cefazolin from

403 92.7% to 82.2%, respectively. It can be deduced that the amount of supporting electrolyte

404 should be optimized to operate the treatment process cost-efficiently for full-scale applications.

405 Considering the importance of this issue, the electrolyte concentration of 50.0 mmol/L was

406 chosen for conducting the next experiments.

407

408 **3.4. Effect of scavenging compounds**

409 The effect of some main scavenging compounds on the degradation efficiency of cefazolin

410 by the CuFeNLDH-CNTs/EF process was evaluated to specify not only the efficiency of the

411 process under adverse conditions but also to determine the role of free oxidizing species in the

412 degradation of target contaminants (Fig. 8). In this regard, inorganic (sodium carbonate) and

413 organic (ethanol (EtOH) and benzoquinone (BQ)) scavenging compounds in the concentration

414 range of 5.0-15.0 mmol/L were added to the cefazolin-contained solution to assess the change

415 in the efficiency of the CuFeNLDH-CNTs/EF process. As illustrated in Fig. 8 (a), the presence

416 of ethanol ($^{\bullet}$OH scavenger) remarkably reduced the degradation efficiency of cefazolin by the

417 EF process according to the following equation [52]:

418 $^{\bullet}OH + C_2H_5OH \rightarrow H_2O + CH_3CHOH^{\bullet}$ (10)
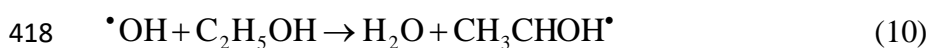
419   At ethanol concentrations of 5.0, 10.0 and 15.0 mmol/L, the degradation efficiencies of

420   62.3%, 53.1% and 43.7% were obtained, respectively; while in the absence of ethanol the

421   degradation efficiency of about 90.0% was achieved within 100 min. The presence of BQ ($O_2^{\bullet-}$

422   scavenger) led to the decreased degradation efficiency of cefazolin (Fig. 8 (b)). The scavenging

423   characteristic of BQ is represented through the following equation [53]:

424     $$BQ + O_2^{\bullet-} \rightarrow O_2 + BQ^{\bullet-} \tag{11}$$

425   BQ is recognized as high potential superoxide anions ($O_2^{\bullet-}$) scavenger [54]. At BQ

426   concentrations of 5.0, 10.0 and 15.0 mmol/L, the degradation efficiencies of 76.0%, 69.7% and

427   59.1% were obtained, respectively. Results of the effect of carbonate ions on the degradation

428   efficiency of cefazolin are displayed in Fig. 8 (c). The decreased degradation efficiency of

429   cefazolin in the presence of carbonate ions is associated with its reaction with $^{\bullet}OH$ radical to

430   produce carbonate radicals with lower oxidation potential as represented in the equation below

431   [17]:

432     $$^{\bullet}OH + CO_3^{2-} \rightarrow CO_3^{\bullet-} + OH^- \tag{12}$$

433   The degradation efficiency of cefazolin decreased from 90.0% to 80.3%, 69.7% and 51.5%

434   in the presence of 5.0, 10.0 and 15.0 mmol/L sodium carbonate, respectively. Based on the

435   results obtained, the presence of ethanol led to the most suppressing effect on the degradation

436   of cefazolin through the CuFeNLDH-CNTs/EF process in comparison with both BQ molecules

437   and carbonate ions. Considering $^{\bullet}OH$ radical scavenging properties of ethanol, indicating the

438   major role of $^{\bullet}OH$ radical in the degradation of antibiotic molecules through the EF process

439   [55], shows that the result is consistent with those obtained and deduced at the end of

440   preliminary experiments data section.

441

442

3.5. Gas injection

Fig. 9 shows the effect of air, O_2, O_3, and Ar injected into the solution on the efficiency of the CuFeNLDH-CNTs/EF process. The addition of O_2 and O_3 enhanced the degradation of cefazolin through the EF process, while Ar sparging led to a significant drop in the degradation efficiency of cefazolin compared with the addition of air. Clearly, the injection of pure oxygen into the bulk solution leads to highly efficient electro-generation of hydrogen peroxide and its conversion to $^\bullet$OH radical in comparison with ambient air. Furthermore, oxygen molecules dissolved in the solution react with Fe ions, generating superoxide anions [56]. As previously mentioned, the addition of BQ demonstrated the role of this type of free radical, but to a lesser extent than $^\bullet$OH radical, in degrading the target pollutant. The highest degradation efficiency was attained when ozone gas was injected into the EF reactor. The interaction of ozone molecules with electro-generated hydrogen peroxide produces $^\bullet$OH radicals in the solution. Furthermore, the rest of as-generated hydrogen peroxide is dissolved in the liquid phase and dissociates into hydroperoxide (HO_2^-) anions, initiating a radical chain reaction to form extra $^\bullet$OH radicals thanks to the reaction with ozone gas [57]. Similar results have been reported by Shen et al. in the case of the catalytic decolorization of wastewater through the ozone/Fenton treatment process [58]. From another point of view, when ozone is injected into the CuFeNLDH-CNTs-equipped EF reactor, recycled Fe^{2+} play catalytic role for the conversion of ozone to $^\bullet$OH radical. The catalytic reaction of ozone with Fe ions also produces FeO^{2+} species, which gradually changes to $^\bullet$OH radical [59]:

$$Fe^{2+} + O_3 \rightarrow FeO^{2+} + O_2 \qquad\qquad (13)$$

$$FeO^{2+} + H_2O \rightarrow Fe^{3+} + {^\bullet}OH + OH^- \qquad\qquad (14)$$
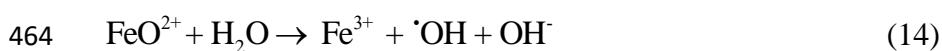
3.6. COD, GC-MS, AAS and stability studies

467   The progress in the mineralization of the target bio-refractory compound was checked

468   via COD analysis over the reaction time of 300 min. Under current intensity of 300.0 mA, the

469   initial COD of the cefazolin-contained solution decreased from 264 mg/L to 79 mg/L by the

470   CuFeNLDH-CNTs/EF process (mineralization efficiency of 70.1%). This result indicated the

471   acceptable destruction and mineralization of the cefazolin antibiotic when it was treated

472   through the CuFeNLDH-CNTs/EF process. The enhanced degradation and mineralization of

473   cefazolin in the EF process equipped with CuFeNLDH-CNTs-coated graphite cathode were

474   mainly the result of the improved catalytic degradation capability of the Fenton process [49].

475   Moreover, the efficient mineralization of the cefazolin improves the potential of the effluent to

476   be treated by the subsequent biological system as a post-treatment method with

477   environmentally friendly effluent. However, the degradation of the target organic compound

478   may result in the formation of unknown organic and inorganic compounds. Thus, GC-MS

479   analysis was carried out to identify the intermediate byproducts generated during the

480   destruction of cefazolin through the CuFeNLDH-CNTs/EF process. The results of GC-MS

481   analysis are displayed in Table 3. According to the byproducts listed in Table 3, cefazolin can

482   be degraded by cleavage of C-S, N=N, N-N, C-N and C-C bonds. In the first step, the parent

483   molecule was disintegrated to hydroxylated cyclic hydrocarbons such as 2-(3-isopropenyl-4-

484   methyl-4-vinylcyclohexyl)-2-propanol, (NE)-N-(2-methyl-5-prop-1-en-2-ylcyclohex-2-en-1-

485   ylidene) hydroxylamine and 2-ethylcyclohexan-1-ol. In the next step, (2E)-3,7-dimethylocta-

486   2,6-dien-1-ol, Octan-4-ol and pentan-2-ol were produced as hydroxylated aliphatic compounds

487   derived from the ring cleavage. Then, various short-chain aliphatic carboxylic acids such as

488   propan-2-ol, 1,1-bis(methylsulfanyl)ethane, acetic acid, 2-hydroxyacetaldehyde and acetamide

489   were produced as the final intermediates. According to the results reported by Le et al., the

490   formation of short-chain aliphatic compounds can result in the detoxification of solution [60].

491   Using evolution of inhibition ratio, they have demonstrated that the toxicity is closely

20

492 associated with the existence of aromatic compounds at the early step of the degradation

493 process rather than short-chain aliphatic compounds detected at the end of the EF process which

494 have insignificant toxicity. Eventually, all of these compounds could be converted to carbon

495 dioxide and water as the final products to achieve mineralization [61]. The AAS technique was

496 also applied to determine the total concentration of Fe and Cu ions dissolved in the cefazolin-

497 contained solution during the CuFeNLDH-CNTs/EF process. The AAS analysis results

498 revealed the release of Fe (0.21 mg/L) and Cu (0.34 mg/L) ions from the modified graphite

499 cathode into the solution during the treatment process. The stability of the CuFeNLDH-CNTs-

500 coated graphite cathode was also investigated by performing ten consecutive experiments.

501 After each experiment, the cathode was washed with distilled water and dried at room

502 temperature. Then, the next experiment was performed under the same experimental

503 conditions. As presented in Fig. S7, there is no remarkable decrement in the performance of

504 CuFeNLDH-CNTs-coated graphite cathode after ten experiments, confirming high stability of

505 the CuFeNLDH-CNTs-modified cathode for the EF process. No more than 4.0% reduction in

506 the removal efficiency of cefazolin was observed at the end of tenth run. This improves the

507 potential of the treatment process to be used in full-scale applications with considerable cost-

508 effectiveness.

509

4. Conclusion

511 CNTs-incorporated CuFeNLDH was immobilized on the surface of the graphite plate to be

512 efficiently applied as a porous cathode for the degradation of cefazolin antibiotic through the

513 EF process. Characterization analyses proved the superior structure of CuFeNLDH/CNTs-

514 coated graphite in comparison with both bare and CNTs-coated cathodes for the reduction of

515 oxygen molecules to hydrogen peroxide as well as decomposition of hydrogen peroxide to $^\bullet$OH

radicals. Increasing the current intensity and supporting electrolyte concentration led to the enhanced destruction of cefazolin through the modified EF process. Conversely, increasing the initial cefazolin concentration along with increasing solution pH resulted in decreased decomposition efficiency. Evaluation of the efficiency of the treatment process in the presence of radical scavenging compounds demonstrated the major role of free oxidizing radicals, especially $^{\bullet}$OH radicals, in the degradation of the target contaminant. These results also showed the high potential of the treatment process to be operated under real conditions. The treatment process had relatively high potential in mineralization of the bio-refractory antibiotic with the release of low amounts of Cu and Fe ions into the bulk solution. The results of GC-MS analysis confirmed the acceptable progress in the conversion of parent compound into the intermediates with low molecular weight and simple structure. Overall, the EF process equipped with CuFeNLDH/CNTs-coated graphite cathode can be utilized as one of the promising Fenton-based AOPs for the decontamination of antibiotic-polluted water streams before being discharged into various ecosystems.

Acknowledgements

References

538 [1] P. Gholami, L. Dinpazhoh, A. Khataee, A. Hassani, A. Bhatnagar, Facile hydrothermal

539 synthesis of novel Fe-Cu layered double hydroxide/biochar nanocomposite with enhanced

540 sonocatalytic activity for degradation of cefazolin sodium, Journal of hazardous materials, 381

541 (2020) 120742.

542 [2] J. Wang, M. Y. Zhang, J. Liu, X. M. Hu, B. S. He, Using a targeted ecopharmacovigilance

543 intervention to control antibiotic pollution in a rural aquatic environment. Science of The Total

544 Environment, 696 (2019) 134007.

545 [3] S. Agarwal, I. Tyagi, V.K. Gupta, M. Sohrabi, S. Mohammadi, A.N. Golikand, A. Fakhri,

546 Iron doped SnO_2/Co_3O_4 nanocomposites synthesized by sol-gel and precipitation method for

547 metronidazole antibiotic degradation, Materials Science and Engineering: C, 70 (2017) 178-

548 183.

549 [4] S. Zhang, I. Khan, X. Qin, K. Qi, Y. Liu, S. Bai, Construction of 1D Ag-AgBr/AlOOH

550 Plasmonic Photocatalyst for Degradation of Tetracycline Hydrochloride, Frontiers in

551 chemistry, 8 (2020) 117.

552 [5] Y.Y. Gurkan, N. Turkten, A. Hatipoglu, Z. Cinar, Photocatalytic degradation of cefazolin

553 over N-doped TiO_2 under UV and sunlight irradiation: Prediction of the reaction paths via

554 conceptual DFT, Chemical Engineering Journal, 184 (2012) 113-124.

555 [6] M. Liu, H. Ni, L. Yang, G. Chen, X. Yan, X. Leng, P. Liu, X. Li, Pretreatment of swine

556 manure containing β-lactam antibiotics with whole-cell biocatalyst to improve biogas

557 production, Journal of Cleaner Production, 240 (2019) 118070.

558 [7] K.A. Rickman, S.P. Mezyk, Kinetics and mechanisms of sulfate radical oxidation of β-

559 lactam antibiotics in water, Chemosphere, 81 (2010) 359-365.

560 [8] M.K. Dail, S.P. Mezyk, Hydroxyl-radical-induced degradative oxidation of β-lactam

561 antibiotics in water: Absolute rate constant measurements, The Journal of Physical Chemistry

562 A, 114 (2010) 8391-8395.

23

563 [9] P. K. Thai, V. N. Binh, P. H. Nhung, P. T. Nhan, N. Q. Hieu, N. T. Dang, N. K. B. Tam,

564 N. T. K. Anh, Occurrence of antibiotic residues and antibiotic-resistant bacteria in effluents of

565 pharmaceutical manufacturers and other sources around Hanoi, Vietnam. Science of the Total

566 Environment, 645 (2018) 393-400.

567 [10] R.D.C. Soltani, M. Mashayekhi, M. Naderi, G. Boczkaj, S. Jorfi, M. Safari, Sonocatalytic

568 degradation of tetracycline antibiotic using zinc oxide nanostructures loaded on nano-cellulose

569 from waste straw as nanosonocatalyst, Ultrasonics Sonochemistry, 55 (2019) 117-124.

570 [11] V. Poza-Nogueiras, E. Rosales, M. Pazos, M.Á. Sanromán, Current advances and trends

571 in electro-Fenton process using heterogeneous catalysts – A review, Chemosphere, 201 (2018)

572 399-416.

573 [12] T. X. H. Le, L. F. Dumée, S. Lacour, M. Rivallin, Z. Yi, L. Kong, M. Bechelany, M.

574 Cretin, Hybrid graphene-decorated metal hollow fibre membrane reactors for efficient electro-

575 Fenton-Filtration co-processes. Journal of membrane science, 587 (2019) 117182.

576 [13] R. Darvishi Cheshmeh Soltani, A.R. Khataee, M. Mashayekhi, Photocatalytic degradation

577 of a textile dye in aqueous phase over ZnO nanoparticles embedded in biosilica

578 nanobiostructure, Desalination and Water Treatment, 57 (2016) 13494-13504.

579 [14] K. Qi, S.-y. Liu, A. Zada, Graphitic carbon nitride, a polymer photocatalyst, Journal of the

580 Taiwan Institute of Chemical Engineers, (2020). https://doi.org/10.1016/j.jtice.2020.02.012

581 [15] J. Gao, Y. Liu, X. Xia, L. Wang, L. Shao, T. Cai, W. Dong, Mechanisms for photo assisted

582 Fenton of synthesized pyrrhotite at neutral pH, Applied Surface Science, 463 (2019) 863-871.

583 [16] T. X. H. Le, M. G. Cowan, M. Drobek, M. Bechelany, A. Julbe, M. Cretin, Fe-nanoporous

584 carbon derived from MIL-53 (Fe): A heterogeneous catalyst for mineralization of organic

585 pollutants, Nanomaterials, 9 (2019) 641.

586 [17] W. Jiang, P. Tang, S. Lu, Y. Xue, X. Zhang, Z. Qiu, Q. Sui, Comparative studies of

587 H_2O_2/Fe(II)/formic acid, sodium percarbonate/Fe(II)/formic acid and calcium

588   peroxide/Fe(II)/formic acid processes for degradation performance of carbon tetrachloride,

589   Chemical Engineering Journal, 344 (2018) 453-461.

590   [18] H. Yang, M. Zhou, W. Yang, G. Ren, L. Ma, Rolling-made gas diffusion electrode with

591   carbon nanotube for electro-Fenton degradation of acetylsalicylic acid, Chemosphere, 206

592   (2018) 439-446.

593   [19] Y. Liu, Q. Fan, J. Wang, Zn-Fe-CNTs catalytic in situ generation of H_2O_2 for Fenton-like

594   degradation of sulfamethoxazole, Journal of hazardous materials, 342 (2018) 166-176.

595   [20] C. Li, G. Zhao, T. Zhang, T. Yan, C. Zhang, L. Wang, F. Jiao, A novel Ag@ TiON/CoAl-

596   layered double hydroxide photocatalyst with enhanced catalytic memory activity for removal

597   of organic pollutants and Cr (VI), Applied Surface Science, 504 (2020) 144352.

598   [21] S.O. Ganiyu, T.X. Huong Le, M. Bechelany, N. Oturan, S. Papirio, G. Esposito, E. van

599   Hullebusch, M. Cretin, M.A. Oturan, Electrochemical mineralization of sulfamethoxazole over

600   wide pH range using FeIIFeIII LDH modified carbon felt cathode: Degradation pathway,

601   toxicity and reusability of the modified cathode, Chemical Engineering Journal, 350 (2018)

602   844-855.

603   [22] N.V. Klassen, D. Marchington, H.C. McGowan, H_2O_2 determination by the I3-method

604   and by $KMnO_4$ titration, Analytical Chemistry, 66 (1994) 2921-2925.

605   [23] I. Talinli, G.J.W.r. Anderson, Interference of hydrogen peroxide on the standard COD test,

606   26 (1992) 107-110.

607   [24] H. Liu, Q. Jiao, Y. Zhao, H. Li, C. Sun, X. Li, Cu/Fe hydrotalcite derived mixed oxides as

608   new catalyst for thermal decomposition of ammonium perchlorate, Materials Letters, 64 (2010)

609   1698-1700.

610   [25] Z. Ai, H. Xiao, T. Mei, J. Liu, L. Zhang, K. Deng, J. Qiu, Electro-Fenton degradation of

611   rhodamine B based on a composite cathode of Cu_2O nanocubes and carbon nanotubes, The

612   Journal of Physical Chemistry C, 112 (2008) 11929-11935.

613 [26] K. Nagase, Y. Zheng, Y. Kodama, J. Kakuta, Dynamic study of the oxidation state of

614 copper in the course of carbon monoxide oxidation over powdered CuO and Cu_2O, Journal of

615 Catalysis, 187 (1999) 123-130.

616 [27] I.C. Pereira, A.S. Duarte, A.S. Neto, J.M.F. Ferreira, Chitosan and polyethylene glycol

617 based membranes with antibacterial properties for tissue regeneration, Materials Science and

618 Engineering: C, 96 (2019) 606-615.

619 [28] Z. Li, J. Xiao, C. Chen, L. Zhao, Z. Wu, L. Liu, D. Cai, Promoting desert biocrust

620 formation using aquatic cyanobacteria with the aid of MOF-based nanocomposite, Science of

621 The Total Environment, (2019) 134824. https://doi.org/10.1016/j.scitotenv.2019.134824.

622 [29] M. Safari, A. Khataee, R. Darvishi Cheshmeh Soltani, R. Rezaee, Ultrasonically facilitated

623 adsorption of an azo dye onto nanostructures obtained from cellulosic wastes of broom and

624 cooler straw, Journal of Colloid and Interface Science, 522 (2018) 228-241.

625 [30] M. B. Khan, X. Cui, G. Jilani, U. Lazzat, A. Zehra, Y. Hamid, B. Hussain, L. Tang, X.

626 Yang, Z. He, Eisenia fetida and biochar synergistically alleviate the heavy metals content

627 during valorization of biosolids via enhancing vermicompost quality, Science of the Total

628 Environment, 684 (2019) 597-609.

629 [31] C.-S. Wu, Y.-L. Liu, K.-Y. Hsu, Maleimide-epoxy resins: preparation, thermal properties,

630 and flame retardance, Polymer, 44 (2003) 565-573.

631 [32] K. Fang, M. Chen, J. Chen, Q. Tian, C. P. Wong, Cotton stalk-derived carbon fiber@ Ni-

632 Al layered double hydroxide nanosheets with improved performances for supercapacitors,

633 Applied Surface Science, 475 (2019) 372-379.

634 [33] S. Mondal, P. Chakraborty, P. Bairi, D.P. Chatterjee, A.K. Nandi, Light induced E–Z

635 isomerization in a multi-responsive organogel: elucidation from 1 H NMR spectroscopy,

636 Chemical Communications, 51 (2015) 10680-10683.

637 [34] R. Darvishi Cheshmeh Soltani, A.R. Khataee, H. Godini, M. Safari, M.J. Ghanadzadeh,

638 M.S. Rajaei, Response surface methodological evaluation of the adsorption of textile dye onto

639 biosilica/alginate nanobiocomposite: thermodynamic, kinetic, and isotherm studies,

640 Desalination and Water Treatment, 56 (2015) 1389-1402.

641 [35] C. Chen, J. Qu, C. Cao, F. Niu, W. Song, CuO nanoclusters coated with mesoporous SiO

642 2 as highly active and stable catalysts for olefin epoxidation, Journal of Materials Chemistry,

643 21 (2011) 5774-5779.

644 [36] Z. Li, M. Shao, H. An, Z. Wang, S. Xu, M. Wei, D.G. Evans, X. Duan, Fast

645 electrosynthesis of Fe-containing layered double hydroxide arrays toward highly efficient

646 electrocatalytic oxidation reactions, Chemical science, 6 (2015) 6624-6631.

647 [37] M. Wang, T. Hou, Z. Shen, X. Zhao, H. Ji, MOF-derived Fe_2O_3: Phase control and effects

648 of phase composition on gas sensing performance, Sensors and Actuators B: Chemical, 292

649 (2019) 171-179.

650 [38] J. Li, Q. Fan, Y. Wu, X. Wang, C. Chen, Z. Tang, X. Wang, Magnetic polydopamine

651 decorated with Mg–Al LDH nanoflakes as a novel bio-based adsorbent for simultaneous

652 removal of potentially toxic metals and anionic dyes, Journal of Materials Chemistry A, 4

653 (2016) 1737-1746.

654 [39] J. Tang, J. Wang, Iron-copper bimetallic metal-organic frameworks for efficient Fenton-

655 like degradation of sulfamethoxazole under mild conditions, Chemosphere, 241 (2020)

656 125002.

657 [40] X. Yang, L. Liu, M. Zhang, W. Tan, G. Qiu, L. Zheng, Improved removal capacity of

658 magnetite for Cr(VI) by electrochemical reduction, Journal of Hazardous Materials, 374 (2019)

659 26-34.

[41] Z. Lv, S. Yang, H. Zhu, L. Chen, N.S. Alharbi, M. Wakeel, A. Wahid, C. Chen, Highly efficient removal of As (V) by using NiAl layered double oxide composites, Applied Surface Science, 448 (2018) 599-608.

[42] M. Li, C. Feng, W. Hu, Z. Zhang, N. Sugiura, Electrochemical degradation of phenol using electrodes of Ti/RuO$_2$–Pt and Ti/IrO$_2$–Pt, Journal of hazardous materials, 162 (2009) 455-462.

[43] F. Deng, H. Olvera-Vargas, O. Garcia-Rodriguez, Y. Zhu, J. Jiang, , S. Qiu, J. Yang, Waste-wood-derived biochar cathode and its application in electro-Fenton for sulfathiazole treatment at alkaline pH with pyrophosphate electrolyte. Journal of Hazardous Materials, 377 (2019) 249-258.

[44] G. Fan, F. Li, D.G. Evans, X. Duan, Catalytic applications of layered double hydroxides: recent advances and perspectives, Chemical Society Reviews, 43 (2014) 7040-7066.

[45] M. Wang, M. Chen, Z. Yang, G. Liu, J. Kee Lee, W. Yang, X. Wang, High-performance and durable cathode catalyst layer with hydrophobic C@PTFE particles for low-Pt loading membrane assembly electrode of PEMFC, Energy Conversion and Management, 191 (2019) 132-140.

[46] L. Qu, Z. Wang, X. Guo, W. Song, F. Xie, L. He, Z. Shao, B. Yi, Effect of electrode Pt-loading and cathode flow-field plate type on the degradation of PEMFC, Journal of Energy Chemistry, 35 (2019) 95-103.

[47] Z. Kang, G. Yang, J. Mo, Y. Li, S. Yu, D.A. Cullen, S.T. Retterer, T.J. Toops, G. Bender, B.S. Pivovar, J.B. Green, F.-Y. Zhang, Novel thin/tunable gas diffusion electrodes with ultra-low catalyst loading for hydrogen evolution reactions in proton exchange membrane electrolyzer cells, Nano Energy, 47 (2018) 434-441.

[48] S. Adhikari, D. Sarkar, G. Madras, Hierarchical design of CuS architectures for visible light photocatalysis of 4-chlorophenol, ACS omega, 2 (2017) 4009-4021.

684 [49] Q. Peng, H. Zhao, L. Qian, Y. Wang, G. Zhao, Design of a neutral photo-electro-Fenton

685 system with 3D-ordered macroporous Fe_2O_3/carbon aerogel cathode: High activity and low

686 energy consumption, Applied Catalysis B: Environmental, 174-175 (2015) 157-166.

687 [50] N.S. Lima, É.M. Souza, N.H. Torres, R. Bergamasco, M.N. Marques, S. Garcia-Segura,

688 O.L. Sanchez de Alsina, E.B. Cavalcanti, Relevance of adjuvants and additives of pesticide

689 commercial formulation on the removal performance of glyphosate by electrochemically

690 driven processes, Journal of Cleaner Production, 212 (2019) 837-846.

691 [51] C. Annabi, F. Fourcade, I. Soutrel, F. Geneste, D. Floner, N. Bellakhal, A. Amrane,

692 Degradation of enoxacin antibiotic by the electro-Fenton process: Optimization,

693 biodegradability improvement and degradation mechanism, Journal of Environmental

694 Management, 165 (2016) 96-105.

695 [52] Z.G. Li, H.J. Zhao, Decomposition of Ethanethiol by a Corona Radical Injection System,

696 in: Materials Science Forum, Trans Tech Publ, 2018, pp. 48-53.

697 [53] Z. Miao, X. Gu, S. Lu, M.L. Brusseau, X. Zhang, X. Fu, M. Danish, Z. Qiu, Q. Sui,

698 Enhancement effects of chelating agents on the degradation of tetrachloroethene in Fe(III)

699 catalyzed percarbonate system, Chemical Engineering Journal, 281 (2015) 286-294.

700 [54] H. Zhao, Y. Wang, Y. Wang, T. Cao, G. Zhao, Electro-Fenton oxidation of pesticides with

701 a novel Fe_3O_4@Fe_2O_3/activated carbon aerogel cathode: High activity, wide pH range and

702 catalytic mechanism, Applied Catalysis B: Environmental, 125 (2012) 120-127.

703 [55] P. Dong, W. Liu, S. Wang, H. Wang, Y. Wang, C. Zhao, In suit synthesis of Fe_3O_4 on

704 carbon fiber paper@polyaniline substrate as novel self-supported electrode for heterogeneous

705 electro-Fenton oxidation, Electrochimica Acta, 308 (2019) 54-63.

706 [56] F. Hao, W. Guo, X. Lin, Y. Leng, A. Wang, X. Yue, L. Yan, Degradation of Acid Orange

707 7 in aqueous solution by dioxygen activation in a pyrite/H_2O/O_2 system, Environmental

708 Science and Pollution Research, 21 (2014) 6723-6728.

709 [57] S.S. Abu Amr, H.A. Aziz, New treatment of stabilized leachate by ozone/Fenton in the

710 advanced oxidation process, Waste Management, 32 (2012) 1693-1698.

711 [58] Y. Shen, Q. Xu, J. Shi, M. Li, Y. Zhang, Optimization and mechanism study of CI Acid

712 Blue 25 wastewater degradation by ozone/Fenton oxidation process: response surface

713 methodology, intermediate products and degradation pathway, Desalination and Water

714 Treatment, 65 (2017) 313-326.

715 [59] Z. Xiong, B. Lai, P. Yang, Insight into a highly efficient electrolysis-ozone process for

716 N,N-dimethylacetamide degradation: Quantitative analysis of the role of catalytic ozonation,

717 fenton-like and peroxone reactions, Water Research, 140 (2018) 12-23.

718 [60] T. Le, T. Nguyen, Z. Yacouba, L. Zoungrana, F. Avril, E. Petit, J. Mendret, V. Bonniol,

719 M. Bechelany, S. Lacour, G. Lesage, M. Cretin, Toxicity removal assessments related to

720 degradation pathways of azo dyes: Toward an optimization of Electro-Fenton treatment,

721 Chemosphere, 161 (2016) 308-318.

722 [61] F. Sopaj, N. Oturan, J. Pinson, F. Podvorica, M.A. Oturan, Effect of the anode materials

723 on the efficiency of the electro-Fenton process for the mineralization of the antibiotic

724 sulfamethazine, Applied Catalysis B: Environmental, 199 (2016) 331-341.

725

726

727 **Figures captions**

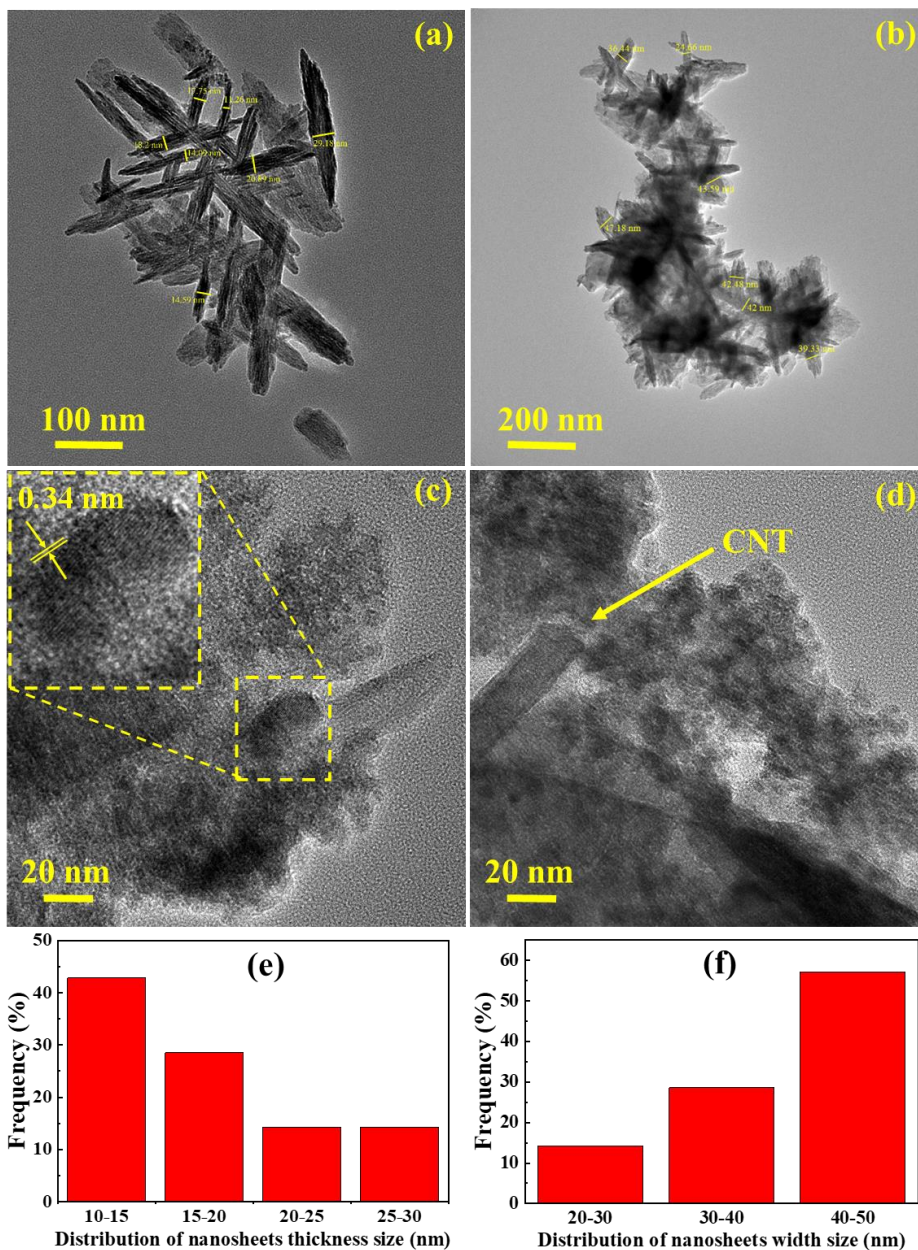728 **Fig. 1.** SEM images of CuFeNLDH (a-d), CNTs (e-h), CuFeNLDH-CNTs (i-l) and

729 CuFeNLDH-CNTs-coated graphite cathode (m-p).

730 **Fig. 2.** HR-TEM images of CuFeNLDH (a and b) and CuFeNLDH-CNTs (c and d), along with

731 thickness (e) and width (f) size distribution plots of CuFeNLDH nanosheets.

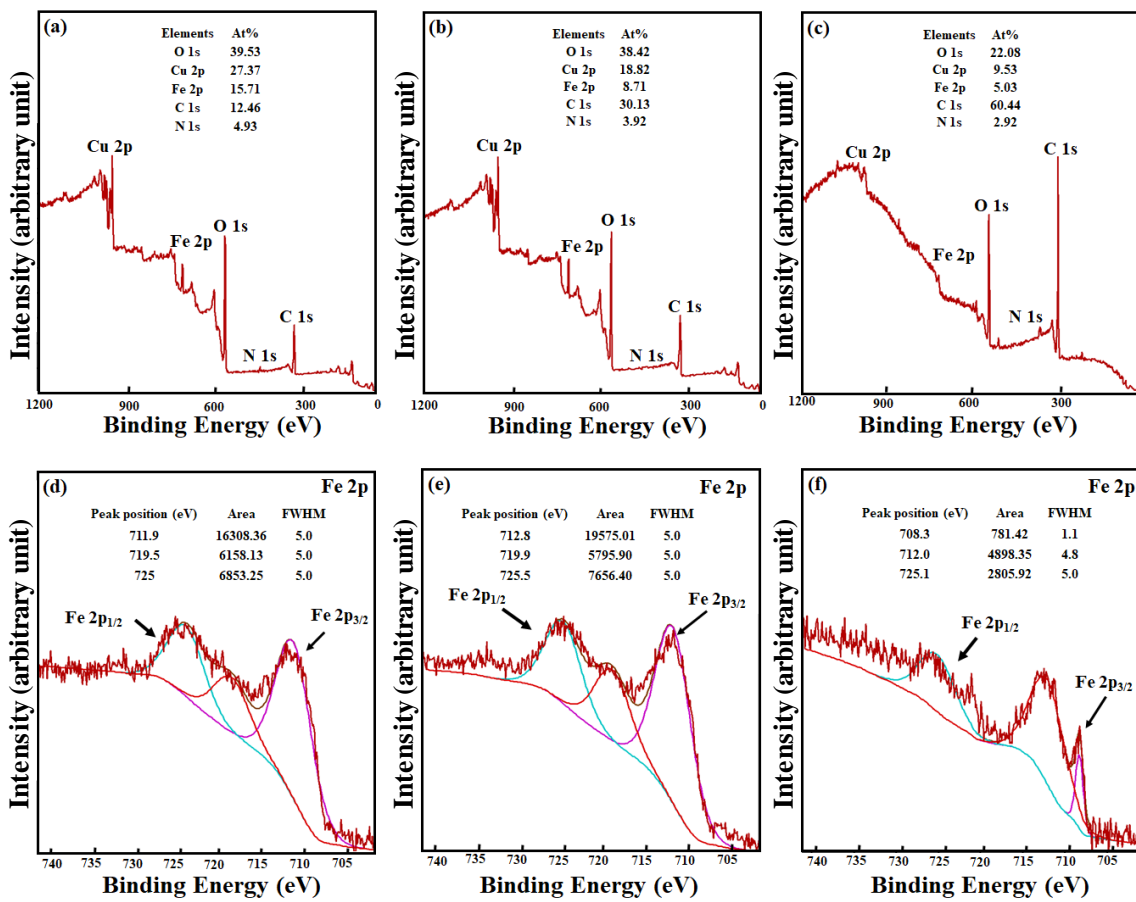**Fig. 3.** XRD patterns of CuFeNLDH (a) CuFeNLDH-CNTs (b) and CuFeNLDH-CNTs modified graphite (c).

Fig. 4. XPS spectra of (a) CuFeNLDH, (b) CuFeNLDH-CNTs and (c) CuFeNLDH-CNTs-coated graphite; together with high resolution Fe 2p (d-f), Cu 2p (g-i) and O 1s (j-l) XPS spectra of CuFeNLDH, CuFeNLDH-CNTs and CuFeNLDH-CNTs-coated graphite samples.

Fig. 5. CV scans in N_2- saturated (a) and (b) O_2-saturated solutions and LSV (b) curves for the bare graphite and CuFeNLDH/CNTs-modified graphite cathodes.

Fig. 6. (a) Comparison of various graphite cathodes, including graphite/NLDH-CNTs (0.10 g), graphite/NLDH-CNTs (0.05 g), graphite/NLDH-CNTs (0.15 g) and graphite/CNTs (0.10 g) for the degradation of cefazolin through EF process; along with the (b) comparison of the amount of H_2O_2 molecules generated on the surface of graphite/CNTs, bare graphite, graphite/NLDH-CNTs (0.05 g) , graphite/NLDH-CNTs (0.10 g) and graphite/NLDH-CNTs (0.15 g) electrodes (Experimental conditions: pH = 6, [cefazolin]$_0$ = 20.0 mg/L, current = 300.0 mA, [Na$_2$SO$_4$] = 50.0 mmol/L and air flow rate = 10.0 L/h).

Fig. 7. (a) The effect of solution pH ([cefazolin]$_0$ = 20.0 mg/L, current = 400.0 mA, [Na$_2$SO$_4$] = 50.0 mmol/L and air flow = 10.0 L/h), (b) applied current (pH = 6.0, [cefazolin]$_0$ = 20.0 mg/L, [Na$_2$SO$_4$] = 50.0 mol/L and air flow = 10.0 L/h), (c) initial concentration of cefazolin (pH = 6.0, current = 300.0 mA, [Na$_2$SO$_4$] = 50.0 mmol/L and air flow = 10.0 L/h), and (d) electrolyte concentration (pH = 6.0, [cefazolin]$_0$ = 20.0 mg/L, current = 300.0 mA and air flow = 10.0 L/h) on the degradation of cefazolin through CuFeNLDH-CNTs/EF process.

Fig. 8. Effects of ethanol (a), benzoquinone (b), and carbonate ions (c) on the degradation of cefazolin by the CuFeNLDH-CNTs/EF process. Experimental conditions: pH = 6, [cefazolin]$_0$ = 20.0 mg/L, current = 300.0 mA, [Na$_2$SO$_4$] = 50.0 mmol/L, air flow rate = 10.0 L/h and [scavenger] = 5.0-15.0 mmol/L.

756   **Fig. 9**. Effect of gas injection (air, O_2, O_3, and Ar) on the degradation of cefazolin by the

757   CuFeNLDH-CNTs/EF process. Experimental conditions: pH = 6.0, [cefazolin]$_0$ = 20.0 mg/L,

758   current = 300.0 mA, [Na_2SO_4] = 50.0 mmol/L, gas flow rate = 10.0 L/h.

759

760

761

762

763

764

765

766

767

768

769

770

771

772

773

774

775

776

777

778

779

780

Research highlights

• Preparation of CuFeNLDH-CNTs incorporated graphite cathode.

• Study of the performance of CuFeNLDH-CNTs attached cathode in electro-Fenton process.

• Achievement of the highest cefazolin degradation through CuFeNLDH-CNTs/EF process.

• Evaluation of the effect of operational parameters on the degradation of cefazolin.

• Identification of degradation intermediates using GC-MS analysis.

Graphical abstract
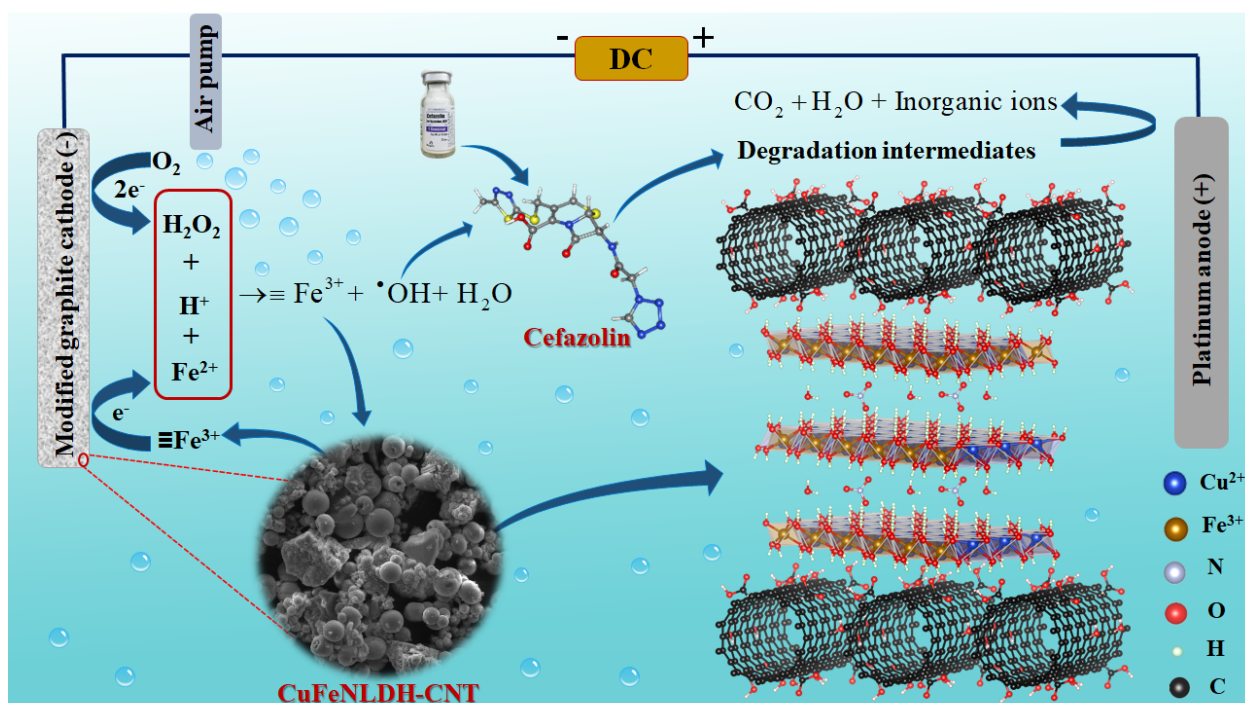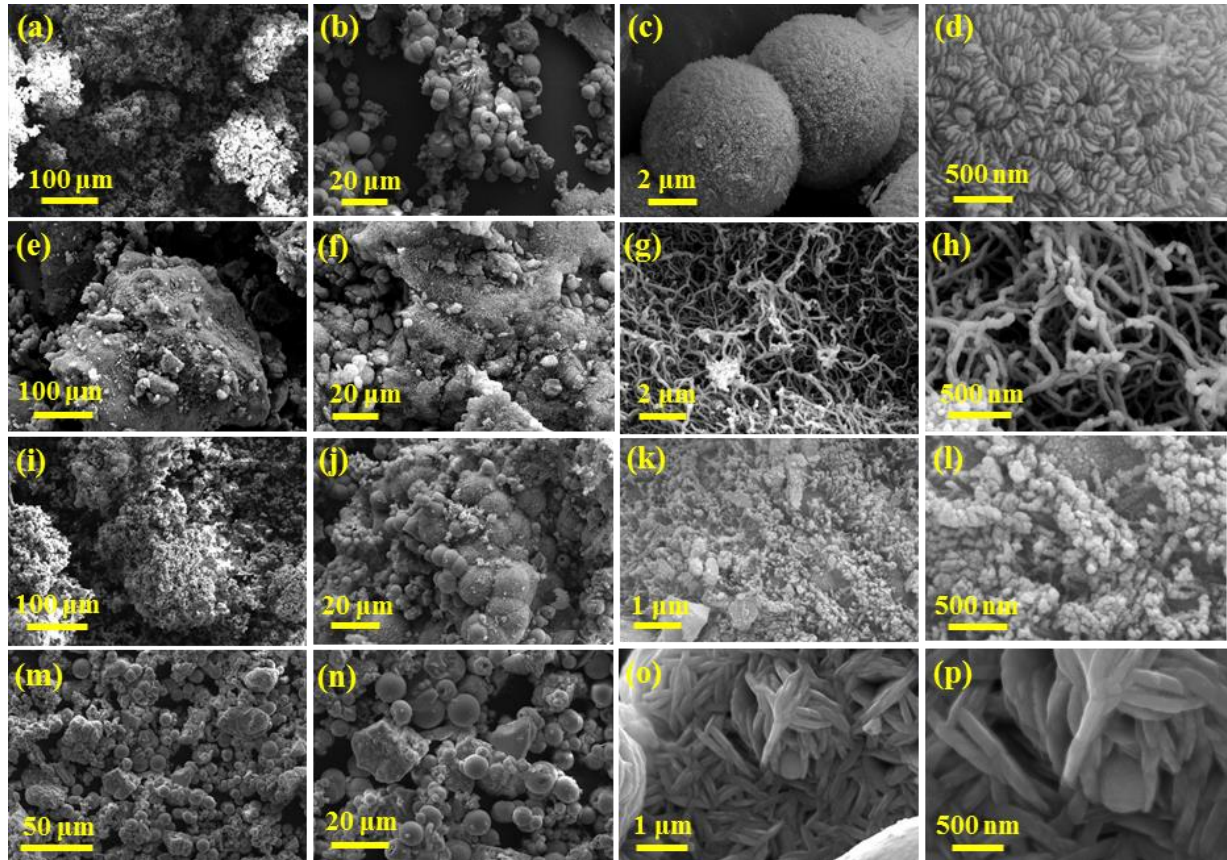
Figures

Fig. 1. SEM images of CuFeNLDH (a-d), CNTs (e-h), CuFeNLDH-CNTs (i-l) and CuFeNLDH-CNTs-coated graphite cathode (m-p).

810

811

812

813

814

815

Fig. 2. HR-TEM images of CuFeNLDH (a and b) and CuFeNLDH-CNTs (c and d), along with thickness (e) and width (f) size distribution plots of CuFeNLDH nanosheets.

819
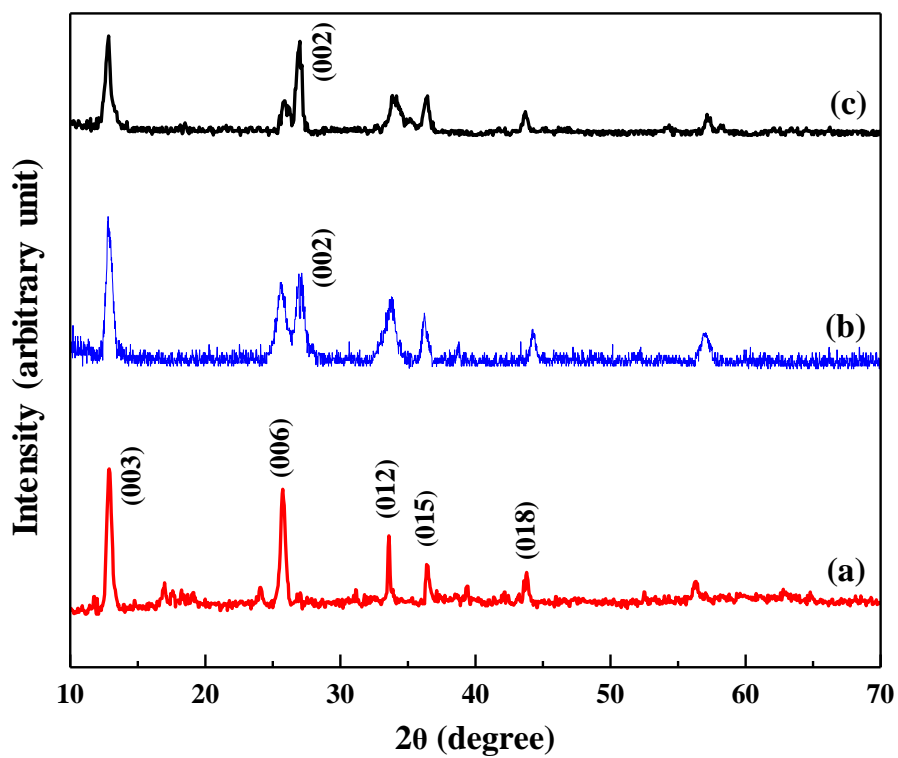
Fig. 3. XRD patterns of CuFeNLDH (a) CuFeNLDH-CNTs (b) and CuFeNLDH-CNTs modified graphite (c).

836

837

838

839

840

841

842

843

844

845

Fig. 4 (a-f)

846

847

848

849

850

851

852

853

854

(g) Cu 2p

Peak position (eV)	Area	FWHM
935.2	38058.00	3.3
942.5	19223.52	4.0
955.4	12562.86	3.1
961.5	25023.63	5.0

Cu 2p$_{3/2}$

Cu 2p$_{1/2}$

(h) Cu 2p

Peak position (eV)	Area	FWHM
935.3	48412.38	2.9
942.7	23765.36	3.8
955.3	14834.20	2.4
962.9	13909.78	2.5

Cu 2p$_{3/2}$

Cu 2p$_{1/2}$

(i) Cu 2p

(j) O 1s

Peak position (eV)	Area	FWHM
531.4	42174.9	2.55

(k) O 1s

Peak position (eV)	Area	FWHM
532.1	61739.9	2.54

(l) O 1s

Peak position (eV)	Area	FWHM
532.2	58299.0	2.16

855

856 **Fig. 4 (g-l)**

857
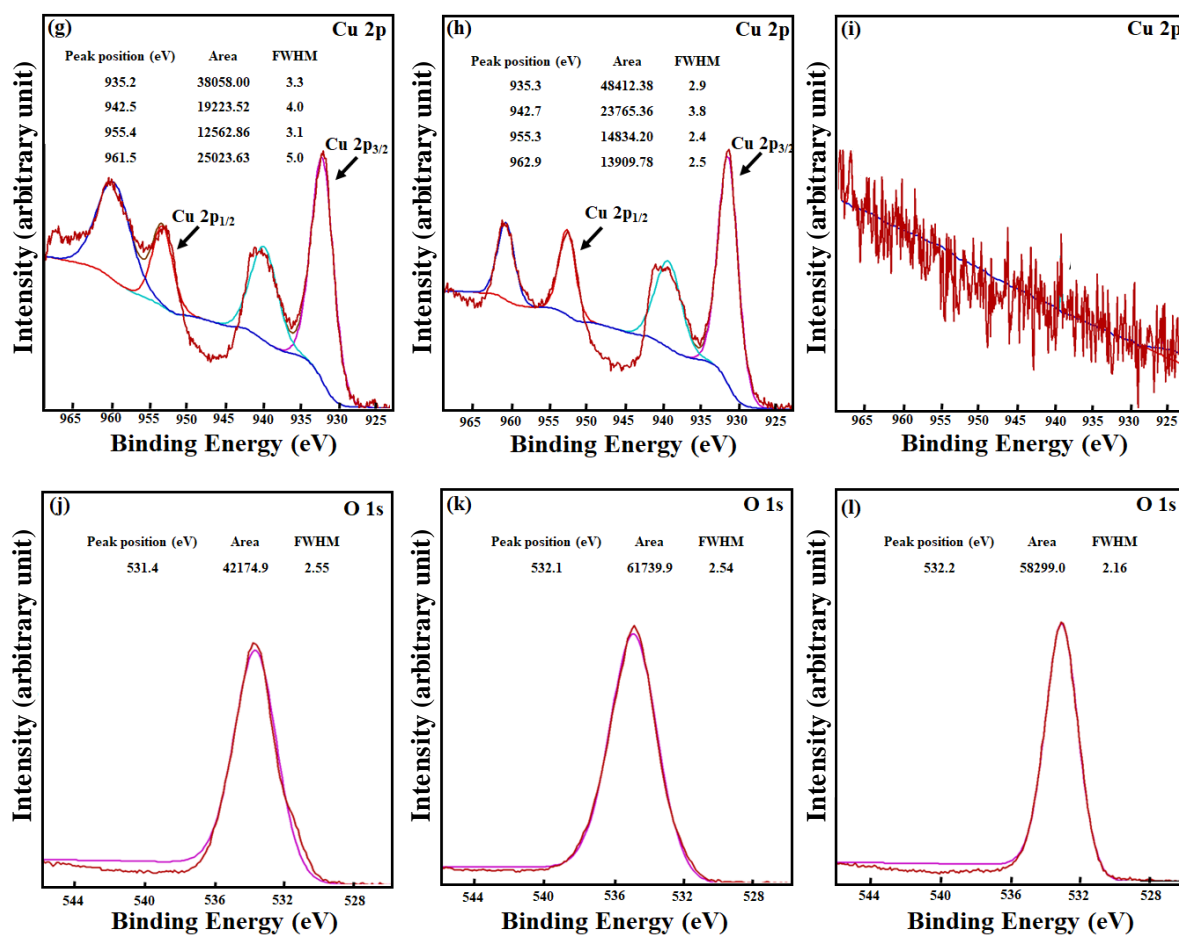
858 **Fig. 4.** XPS spectra of (a) CuFeNLDH, (b) CuFeNLDH-CNTs and (c)
859 CuFeNLDH-CNTs-coated graphite; together with high resolution Fe 2p (d-f),
860 Cu 2p (g-i) and O 1s (j-l) XPS spectra of CuFeNLDH, CuFeNLDH-CNTs and
861 CuFeNLDH-CNTs-coated graphite samples.

862

863

864
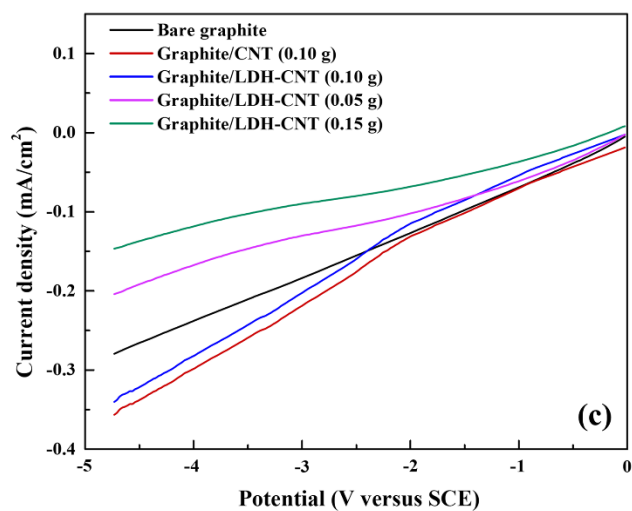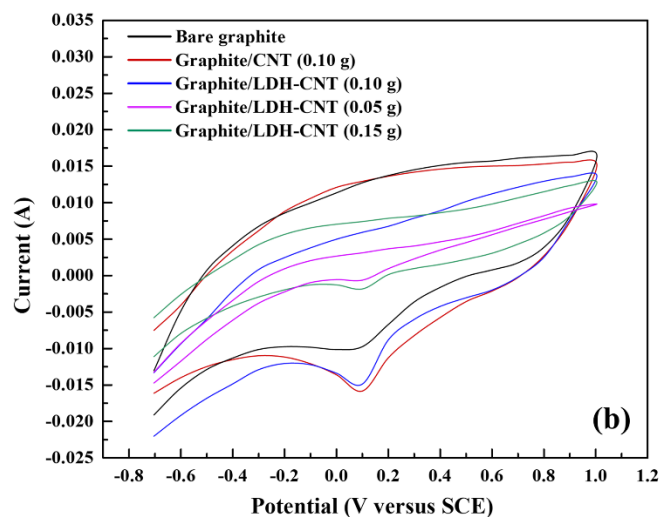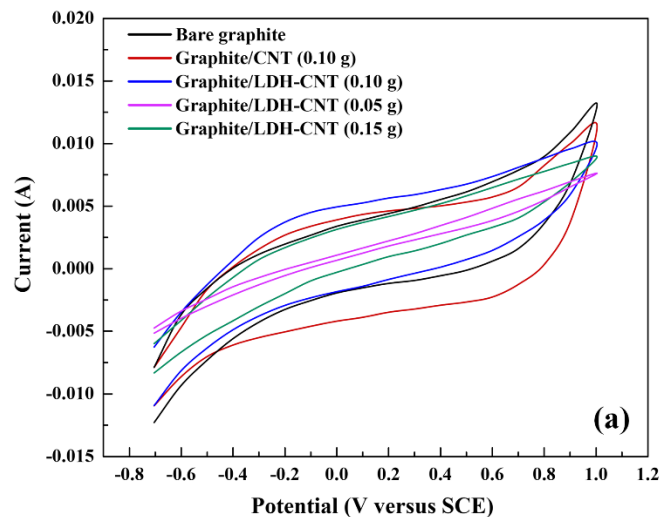
865

866

867   **Fig. 5.** CV scans in N_2-saturated (a) and O_2-saturated (b) solutions and LSV
868   curves (c) for the bare graphite and CuFeNLDH/CNTs-modified graphite
869   cathodes.

870
871
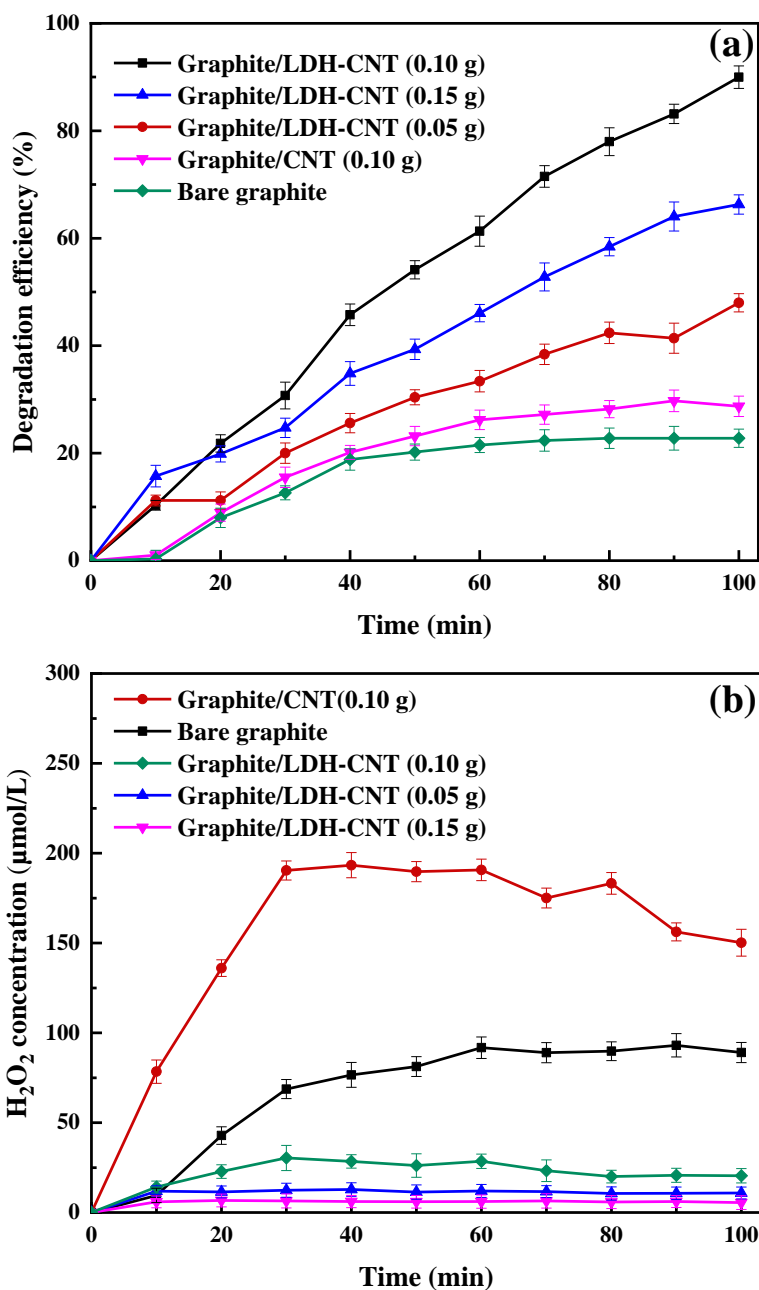
872

Fig. 6. (a) Comparison of various graphite cathodes, including graphite/NLDH-CNTs (0.10 g), graphite/NLDH-CNTs (0.05 g), graphite/NLDH-CNTs (0.15 g) and graphite/CNTs (0.10 g) for the degradation of cefazolin through EF process; along with the (b) comparison of the amount of H_2O_2 molecules generated on the surface of graphite/CNTs, bare graphite, graphite/NLDH-CNTs (0.05 g) , graphite/NLDH-CNTs (0.10 g) and graphite/NLDH-CNTs (0.15 g) electrodes (Experimental conditions: pH = 6, [cefazolin]$_0$ = 20.0 mg/L, current = 300.0 mA, [Na$_2$SO$_4$] = 50.0 mmol/L and air flow rate = 10.0 L/h).

880

881

Fig. 7. (a) The effect of solution pH ([cefazolin]$_0$ = 20.0 mg/L, current = 400.0 mA, [Na$_2$SO$_4$] = 50.0 mmol/L and air flow = 10.0 L/h), (b) applied current (pH = 6.0, [cefazolin]$_0$ = 20.0 mg/L, [Na$_2$SO$_4$] = 50.0 mol/L and air flow = 10.0 L/h), (c) initial concentration of cefazolin (pH = 6.0, current = 300.0 mA, [Na$_2$SO$_4$] = 50.0 mmol/L and air flow = 10.0 L/h), and (d) electrolyte concentration (pH = 6.0, [cefazolin]$_0$ = 20.0 mg/L, current = 300.0 mA and air flow = 10.0 L/h) on the degradation of cefazolin through CuFeNLDH-CNTs/EF process.

888

889

890

891

892

893

Fig. 8. Effects of ethanol (a), benzoquinone (b), and carbonate ions (c) on the degradation of cefazolin by the CuFeNLDH-CNTs/EF process. Experimental conditions: pH = 6, $[cefazolin]_0 = 20.0$ mg/L, current = 300.0 mA, $[Na_2SO_4] = 50.0$ mmol/L, air flow rate = 10.0 L/h and [scavenger] = 5.0-15.0 mmol/L.

894
895
896
897
898
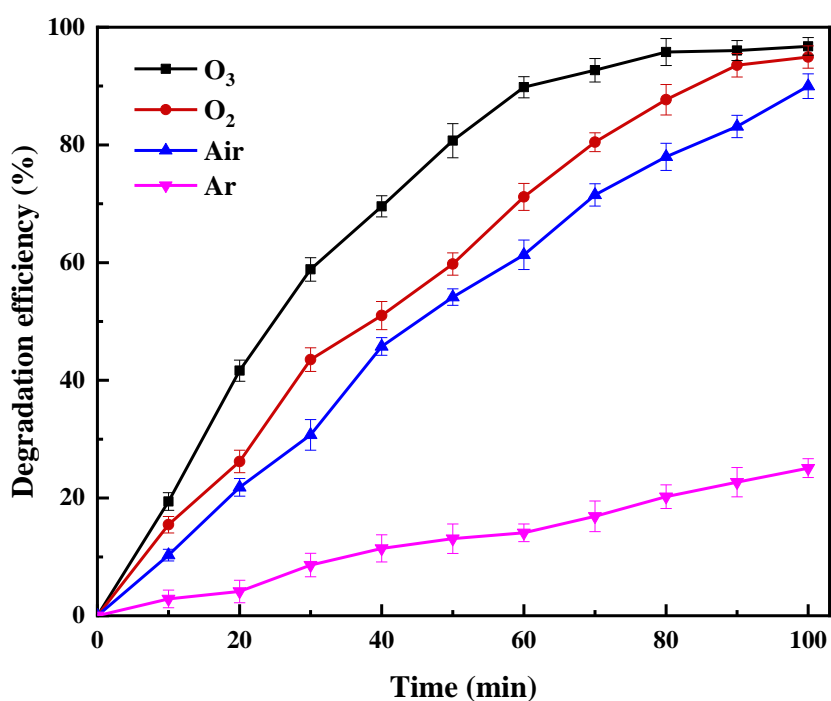
Fig. 9. Effect of gas injection (air, O_2, O_3, and Ar) on the degradation of cefazolin by the CuFeNLDH-CNTs/EF process. Experimental conditions: pH = 6.0, [cefazolin]$_0$ = 20.0 mg/L, current = 300.0 mA, [Na$_2$SO$_4$] = 50.0 mmol/L, gas flow rate = 10.0 L/h.

922 **Tables**

923

924 **Table 1**. Characteristics of cefazolin.

Name	Chemical structure	Molecular formula	λ_{max} (nm)	M_w (g/mol)
Cefazolin		$C_{14}H_{14}N_8O_4S_3$	260	454.498

925

926

927

928

929

930

931

932

933

934

935

936

937

938

939

940

941

942

943 **Table 2.** Identified intermediate byproducts generated during the degradation of cefazolin by

944 the heterogeneous EF process. Experimental conditions: pH = 6.0, current = 300.0 mA,

945 [cefazolin]$_0$ = 20.0 mg/L, [Na$_2$SO$_4$] = 50.0 mmol/L, and air flow rate = 10.0 L/h.

No.	Compound name	Structure	Retention time (min)	Main fragments
1	2-(4-methyl-3-(prop-1-en-2-yl)-4-vinylcyclohexyl)propan-2-ol		15.678	**69**, 75, 82, 93, 148
2	(2E)-3,7-dimethylocta-2,6-dien-1-ol		12.216	68, **69**, 121, 148
3	2-Cyclohexen-1-one, 2-methyl-5-(1-methylethenyl)-, oxime		10.163	54, **82**, 93, 108, 207
4	Propan-2-ol		7.167	59, 73, **75**, 147, 187
5	Pentan-2-ol		7.03	59, 75, 147, **187**
6	Octan-4-ol		7.012	73, **75**, 147
7	1,1-bis(methylthio)ethane		6.912	59, 73, **75**, 147, 149
8	2-Ethylcyclohexanol		3.938	68, **69**, 93, 148
9	Acetic acid		3.805	59, **75**, 76, 116
10	2-Hydroxyacetaldehyde		3.339	73, 75, **76**, 116

45

| 11 | Acetamide | | 3.150 | 59, 73, **75**, 76, 116 |

946

947

948

949

950

951

952

953

954

955

956

957

958

959

960

961

962

963

964

965

966

967

968

Supplementary data

970

971

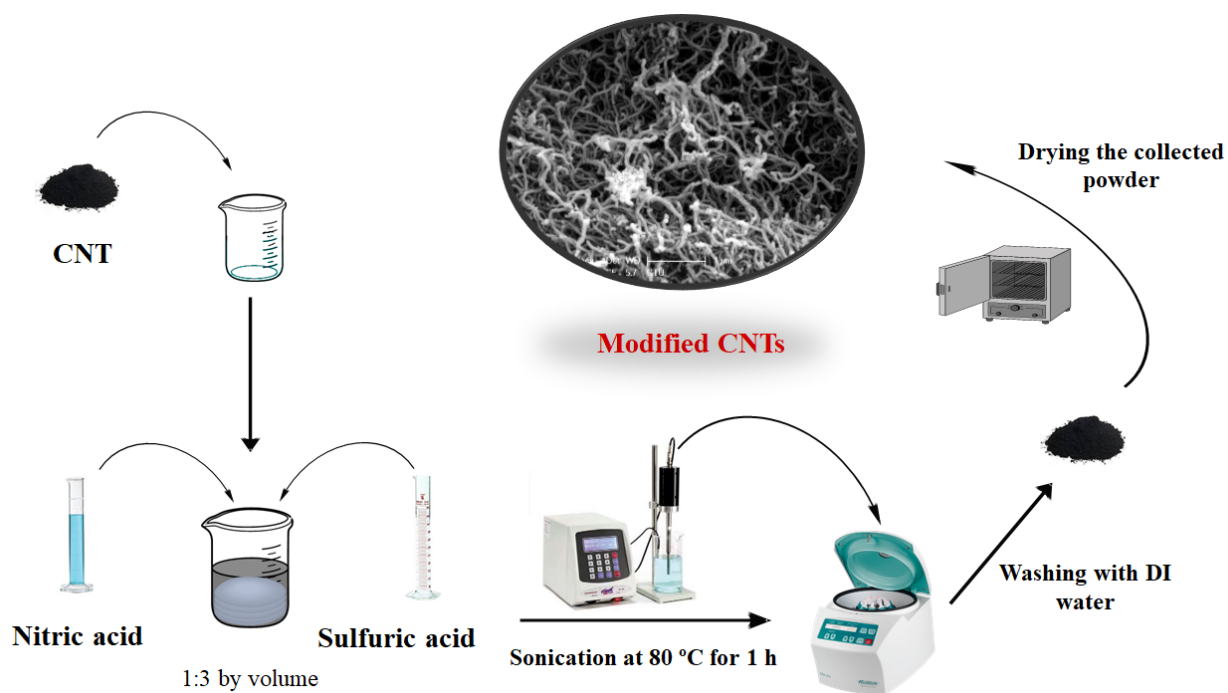972

973

974

975

CNT

Modified CNTs

Drying the collected powder

Nitric acid　　　　**Sulfuric acid**

1:3 by volume

Sonication at 80 ºC for 1 h

Washing with DI water

Fig. S1. Schematic design for the modification of CNTs.

979

980

981

982

983

984

985

986

987

988

989

990

991

992

993

994
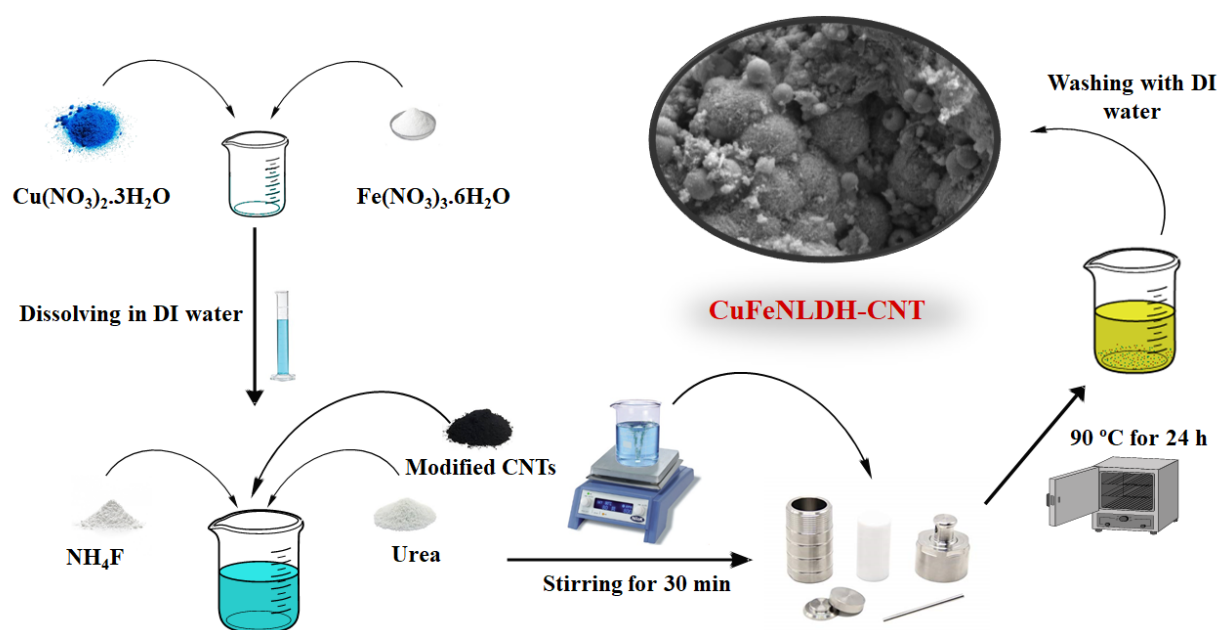
Fig. S2. Schematic diagram for synthesis of CuFeNLDH-CNTs.
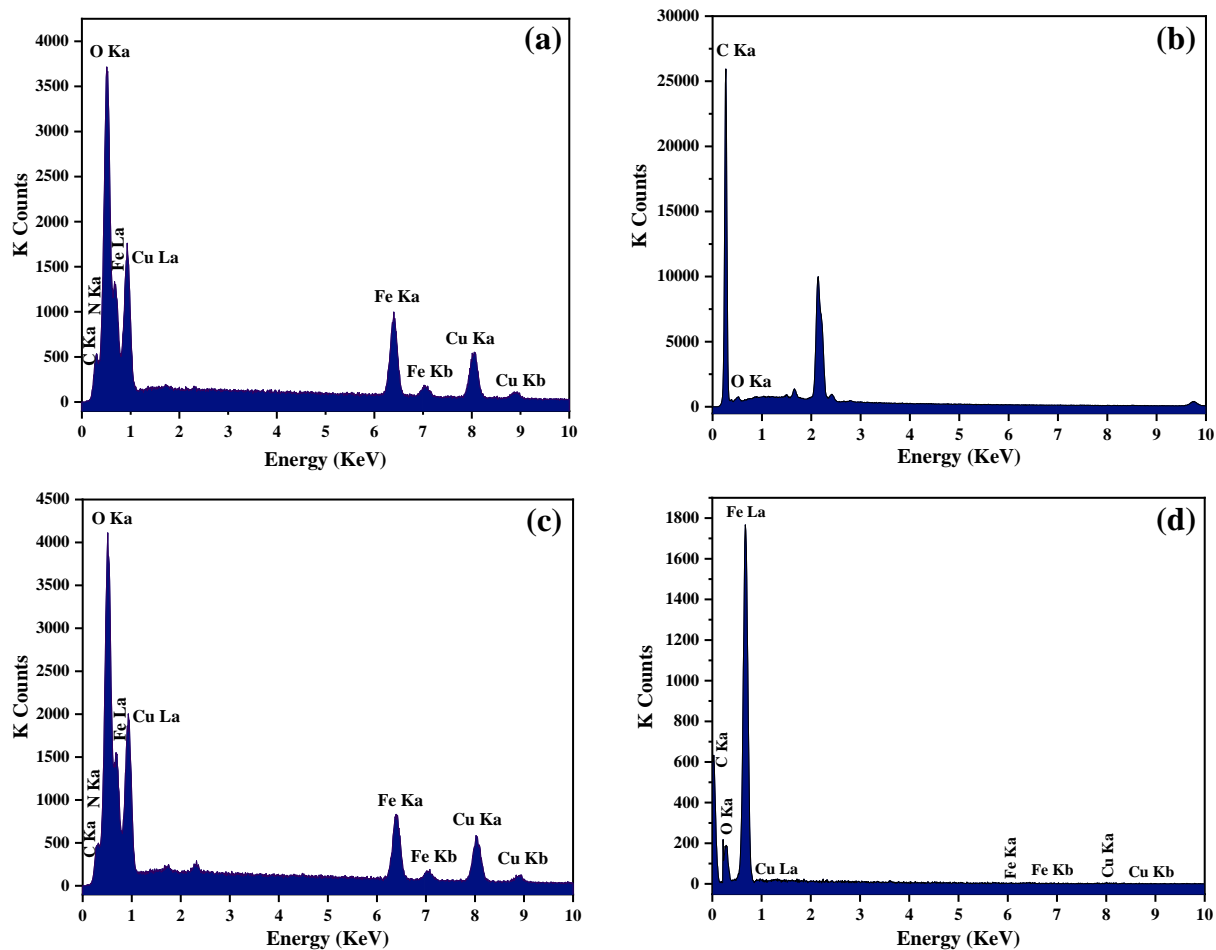
996

997

998

999

1000

1001

1002

1003

1004

1005

1006

1007

1008

1009

1010

1011

1012

1013

1014 **Fig. S3.** Schematic diagram for immobilization of CuFeNLDH-CNTs nanocomposite on the
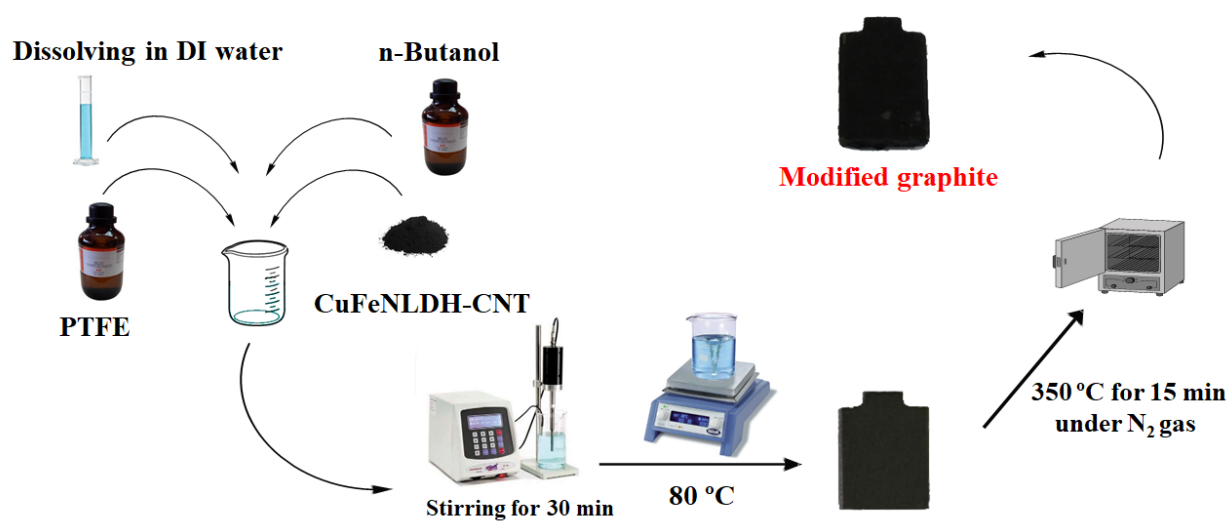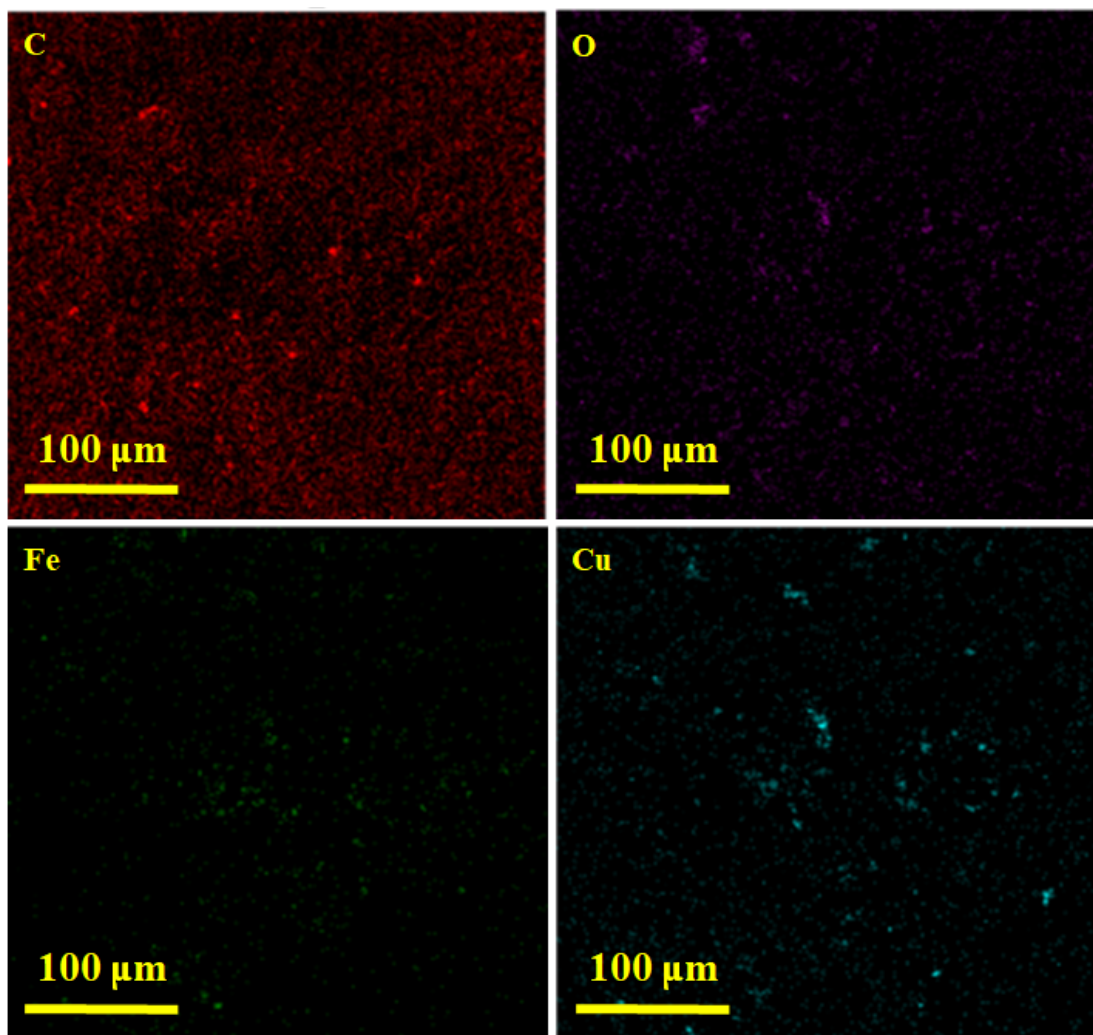
1015 surface of graphite plate.

1016

1017

1018

1019

1020

1021

1022

1023

1024

1025

1026

1027

1028

1029 **Fig. S4.** EDX spectra of CuFeNLDH (a) CNTs (b), CuFeNLDH-CNTs (c) and modified

1030 graphite (d).

1031

1032

1033

1034
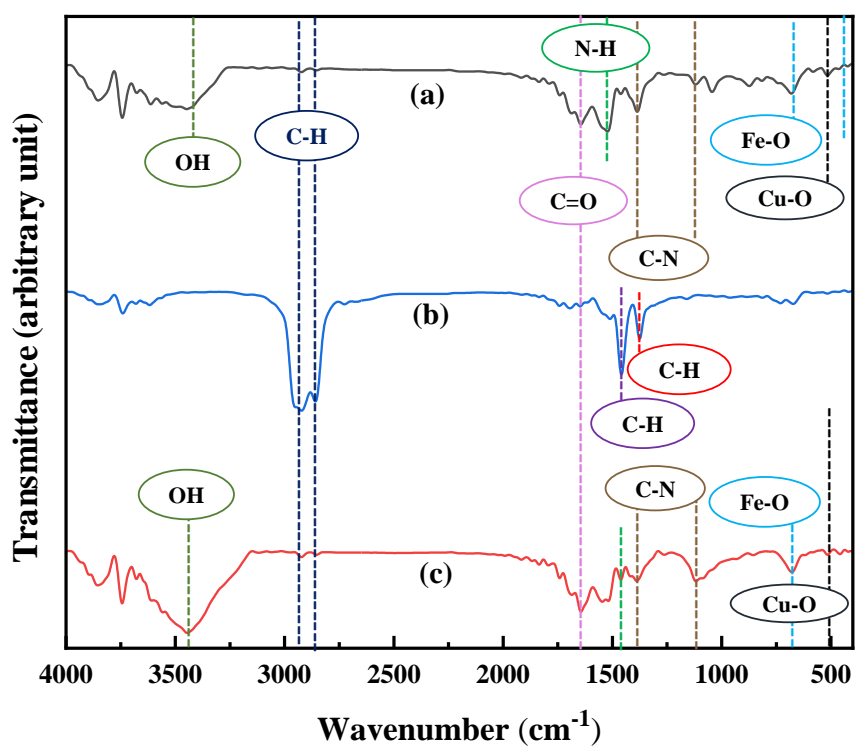
1035

1036

1037

1038

1039

1040

1041

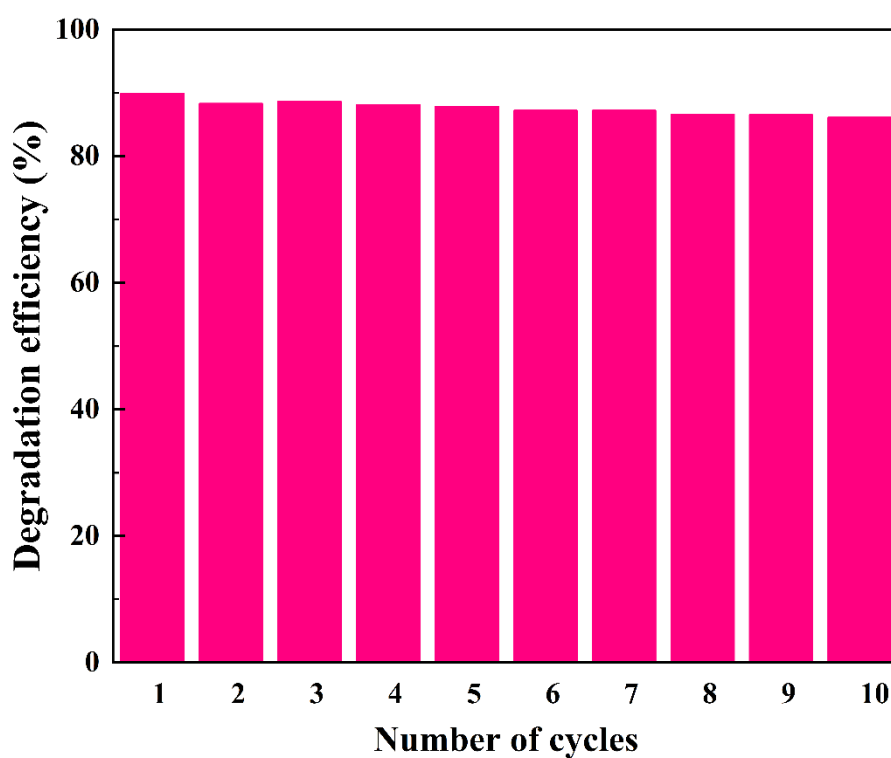**Fig. S5.** Elemental mapping images of CuFeNLDH-CNTs-coated -coated graphite cathode.

1043

1044

1045

1046

1047

1048

1049

1050

1051

1052

1053

1054

Fig. S6. FT-IR spectra of CuFeNLDH (a) CNTs (b) and CuFeNLDH/CNTs (c).

1055

1056

1057

1058

1059

1060

1061

1062

1063

1064

1065

1066

1067

1068

1069

Fig. S7. Cyclic stability of CuFeNLDH-CNTs-coated graphite cathode for CFZ degradation through EF process; Experimental condition: pH = 6, $[cefazolin]_0$ = 20.0 mg/L, current = 300.0 mA, $[Na_2SO_4]$ = 0.05 mol/L and air flow rate = 10.0 L/h.

1074